

# Observation of a superradiant phase transition with emergent cat states

Ri-Hua Zheng,<sup>1,\*</sup> Wen Ning,<sup>1,\*</sup> Ye-Hong Chen,<sup>1,2,3,\*</sup> Jia-Hao Lü,<sup>1</sup> Li-Tuo Shen,<sup>1</sup> Kai Xu,<sup>4,5</sup> Yu-Ran Zhang,<sup>6,2,3</sup> Da Xu,<sup>7</sup> Hekang Li,<sup>5</sup> Yan Xia,<sup>1</sup> Fan Wu,<sup>1</sup> Zhen-Biao Yang,<sup>1,†</sup> Adam Miranowicz,<sup>2,8</sup> Neill Lambert,<sup>2</sup> Dongning Zheng,<sup>4,5</sup> Heng Fan,<sup>4,5</sup> Franco Nori,<sup>2,3,9,‡</sup> and Shi-Biao Zheng<sup>1,§</sup>

<sup>1</sup>*Fujian Key Laboratory of Quantum Information and Quantum Optics,*

*College of Physics and Information Engineering, Fuzhou University, Fuzhou, Fujian 350108, China*

<sup>2</sup>*Theoretical Quantum Physics Laboratory, RIKEN Cluster for Pioneering Research, Wako-shi, Saitama 351-0198, Japan*

<sup>3</sup>*Quantum Information Physics Theory Research Team,*

*RIKEN Center for Quantum Computing (RQC), Wako-shi, Saitama 351-0198, Japan*

<sup>4</sup>*Institute of Physics and Beijing National Laboratory for Condensed Matter Physics, Chinese Academy of Sciences, Beijing 100190, China*

<sup>5</sup>*CAS Center for Excellence in Topological Quantum Computation,*

*University of Chinese Academy of Sciences, Beijing 100190, China*

<sup>6</sup>*School of Physics and Optoelectronics, South China University of Technology, Guangzhou 510640, China*

<sup>7</sup>*Interdisciplinary Center of Quantum Information, State Key Laboratory of Modern Optical*

*Instrumentation and Zhejiang Province Key Laboratory of Quantum Technology and Device,*

*School of Physics, Zhejiang University, Hangzhou 310027, China*

<sup>8</sup>*Institute of Spintronics and Quantum Information, Faculty of Physics, Adam Mickiewicz University, 61-614 Poznań, Poland*

<sup>9</sup>*Department of Physics, University of Michigan, Ann Arbor, Michigan 48109-1040, USA*

Superradiant phase transitions (SPTs) are important for understanding light-matter interactions at the quantum level, and play a central role in criticality-enhanced quantum sensing. So far, SPTs have been observed in driven-dissipative systems, but the emergent light fields did not show any nonclassical characteristic due to the presence of strong dissipation. Here we report an experimental demonstration of the SPT featuring the emergence of a highly nonclassical photonic field, realized with a resonator coupled to a superconducting qubit, implementing the quantum Rabi model. We fully characterize the light-matter state by Wigner matrix tomography. The measured matrix elements exhibit quantum interference intrinsic of a photonic mesoscopic superposition, and reveal light-matter entanglement.

The Dicke model [1, 2], involving a quantized light field coupled to  $N$  two-level atoms, represents a paradigm for realizing exotic quantum phenomena that are absent in semi-classical light-matter systems. Superradiant phase transitions (SPTs) are one of the most famous examples [3–5], where the behavior of the light is sharply changed when the light-matter coupling strength becomes comparable to their frequencies. Under equilibrium conditions, the SPT features a sudden buildup of a photonic field that is highly entangled with the atoms in a mesoscopic superposition [5]. In addition to its fundamental appeal, such cat states can be used as an intrinsically-protected qubit for fault-tolerant quantum computation [6] and as a resource for quantum enhanced metrology [7]. The equilibrium SPT has been attracting enduring attention since the 1970s, but its experimental demonstration still remains very challenging. This is mainly because the neglected square of the vector potential actually increases quadratically with the coupling strength and the photon number, which prohibits the occurrence of SPTs, known as the no-go theorem [8]. Over the past decade, breakthrough experiments have been reported for dynamical realizations of SPTs with a collection of driven atoms trapped in an optical cavity [9–16], whose photonic dissipation enabled the phase transition to be monitored by measuring the output field. This dissipation, however, at the same time obscured the quantum coherence of the light, as well as the light-matter entanglement inherent in the superradiant phase (SP).

Although originally proposed in the thermodynamic limit  $N \rightarrow \infty$ , SPTs can actually occur in the quantum Rabi

model (QRM), which only involves a single atom coupled to a light field [17, 18]. Recent years have witnessed remarkable advances in simulations of the Rabi model in different systems, where the photonic mode was emulated by a phononic mode of a trapped ion [19, 20], while the light field coupling the ion's internal and external degrees of freedom is classical. Circuit QED represents an alternative excellent platform for exploring quantized light-matter systems in regimes that are inaccessible with conventional cavity QED [21–24], and for simulating controlled many-body dynamics [25, 26]. In particular, recent experiments [27] have demonstrated some spectroscopic signatures in the deep-strong coupling regimes. The long coherence times of the superconducting qubits and the microwave photons makes circuit QED promising for realizing SPT produced by a unitary process, in distinct contrast with ultracold-atoms-based cavity QED systems [9–16], where SPT was realized in a dissipative-driven manner. This unitary nature, together with the ability to individually control and measure the superconducting qubits, enables the exploration of nonclassical characteristics associated with the SPT, such as the qubit-resonator entanglement and phase-space quantum interference behaviors of the resonator.

Theoretical investigations indicate that the no-go theorem can be circumvented in circuit QED systems [28]. However, the approximation for describing a superconducting artificial atom as a qubit may break down when increasing the coupling strength due to the limited anharmonicity [29], which prohibits the occurrence of dynamical signatures of the Rabi model, even when the deep-strong regime is reached [27]. To

overcome this problem, it was proposed to effectively transform the Jaynes-Cummings model into the Rabi model, by applying continuous microwave fields to the qubit [22, 30] or by introducing a two-photon drive to the resonator [31–34]. Following these approaches, some important features predicted by the Rabi model have been observed [35, 36]. Despite these advancements, so far the SPT of a real radiant field with non-classical features has not been reported in any system.

Here we report a realization of the first-order SPT of a quantum light field manifested by an emergent cat state. Our demonstration involves a resonator and a superconducting qubit coupled at the second sideband of a strong parametric modulation produced by an ac magnetic flux. This strong longitudinal modulation, together with a weak modulation and a transverse microwave driving, enables the realization of an effective Rabi model with a controllable coupling-frequency ratio. We fully describe the nonclassical behavior of the system by measuring the Wigner function matrix of the joint qubit-resonator system, which contains full information about its state. The measured matrix elements unambiguously demonstrate that the photonic field emergent in the SP is in a quantum superposition of two quasi-classical states that are degenerate in amplitude but have opposite phases. These results bridge the gap between the phase transitions predicted in closed quantum systems and those observed in real macroscopic systems, which is critical to understanding how a symmetry-broken macroscopic order emerges from the dynamics governed by a symmetry-preserving Hamiltonian.

The theoretical model includes a quantized light field stored in a resonator coupled to a qubit, e.g., a tunable Xmon qubit [see Fig. 1(a)], whose transition frequency is periodically modulated [37] as  $\omega_q = \omega_0 + \varepsilon_1 \cos(\nu_1 t) + \varepsilon_2 \cos(\nu_2 t)$ , where  $\omega_0$  corresponds to the mean transition frequency of the qubit, and  $\varepsilon_{1,(2)}$  [ $\nu_{1,(2)}$ ] are the corresponding modulation amplitudes (frequencies). In addition to these longitudinal modulations, the qubit is transversely driven by an external field at the frequency  $\omega_0$  with an amplitude  $K$ . The system dynamics is described by the Hamiltonian

$$H = \hbar \left[ \omega_p a^\dagger a + \frac{\omega_q}{2} \sigma_z + (\lambda a^\dagger \sigma_- + K e^{i\omega_0 t} \sigma_- + \text{h.c.}) \right], \quad (1)$$

where  $a^\dagger$  ( $a$ ) denotes the creation (annihilation) operator for the photonic field with frequency  $\omega_p$ ,  $\lambda$  is the qubit-resonator coupling strength,  $\sigma_z = |e\rangle\langle e| - |g\rangle\langle g|$ , and  $\sigma_- = |g\rangle\langle e|$  are Pauli operators for the qubit. Under the condition  $\nu_1 \gg \lambda, K, \delta$  with  $\delta = \omega_p - \omega_0 - 2\nu_1$ , the resonator interacts with the qubit at the second sideband associated with the first modulation, while the drive works at the carrier, as shown in Fig. 1(a).

The effective dynamics can be well understood in terms of the motion of a spin-1/2 in magnetic fields. As shown in Fig. 1(b), the transverse drive can be thought of as a static magnetic field of strength  $B_0 = 2K J_0(\mu)$  along the  $x$ -axis, forcing the Bloch vector of the qubit to make a Larmor precession with angular frequency  $B_0$ , where  $J_m(\mu)$  denotes the  $m$ th Bessel function of the first kind with  $\mu = \varepsilon_1/\nu_1$ . The sec-

ond longitudinal modulation acts as the combination of two components:  $B_1^\pm$  that have the same amplitude  $|B_1^\pm| = \varepsilon_2/4$ , but rotate with opposite angular velocities  $\pm\nu_2$  on the  $yz$ -plane. On the other hand, the quantized light field behaves like a magnetic field with the  $x$ - and  $y$ -components

$$B_2^x = 2\eta (a + a^\dagger), \quad B_2^y = 2i\eta (a^\dagger - a), \quad (2)$$

where  $\eta = \lambda J_2(\mu)/2$ . When  $B_0 = \nu_2 \gg B_1, B_2^{x(y)}$ , in the framework coinciding with the Larmor precession, the components  $B_1^-$  and  $B_2^y$  can be discarded due to fast rotations [see Fig. 1(c)]. Consequently, the dynamics can be described by the effective quantum Rabi Hamiltonian ( $\hbar = 1$ )

$$H_R = \frac{1}{2} \Omega \sigma_z + \delta a^\dagger a + \eta \sigma_x (a + a^\dagger), \quad (3)$$

which is obtained by subsequently performing the transformations  $\exp \left[ i \int_0^t H_0 dt \right]$  and  $\exp (i B_0 \sigma_x t / 2)$  and neglecting the fast-oscillating terms (see Supplementary Material Sec. S1 A [38]), where  $\Omega = \varepsilon_2/2$  and

$$H_0 = (\omega_0 + 2\nu_1) a^\dagger a + \frac{1}{2} [\omega_0 + \varepsilon_1 \cos(\nu_1 t)] \sigma_z. \quad (4)$$

We note that the synthesized qubit-resonator system corresponds to an isomorphism of the QRM [52], where the effective counter-rotating-wave coupling is produced by the external drive, but not inherent in the qubit-resonator interaction as in the QRM without driving. With this realization, the system frequencies are replaced by the transverse driving detuning and the longitudinal modulation amplitude, which can be easily tuned. Consequently, the critical point of the SPT can be reached in the effective QRM without requiring the qubit-resonator coupling to be comparable to the system frequencies, thereby circumventing the restriction of the no-go theorem.

Our experimental device possesses a bus resonator and five frequency-tunable Xmon qubits, one of which is used as the test qubit for realizing the QRM. Before the experiment, each qubit is initialized to its ground state. The experiment starts by tuning the test qubit to the operating frequency  $\omega_0/2\pi = 5.18$  GHz, where a continuous microwave  $K$  is applied. This transverse driving, together with the two longitudinal sine modulations, effectively realizes the Rabi Hamiltonian of Eq. (3). The experimental details are shown in Supplementary Material Sec. S2 [38], including experimental setup, device parameters, and pulse sequence. During the quenching process where the ratio  $\xi = 2\eta/\sqrt{\Omega\delta}$  is slowly increased, all the qubits, except the test one, remain in their ground states as they are detuned from the resonator by an amount about twenty times larger than the corresponding qubit-resonator coupling strengths. Such a process is realized by varying the control parameter as  $\xi(t) = 1.5 - \exp(-8t/t_f)$ , with  $t_f = 2$   $\mu$ s.

To characterize the photon-number populations after a pre-set quench time, the microwave drive and the frequency modulations are switched off, so that the test qubit is effectively

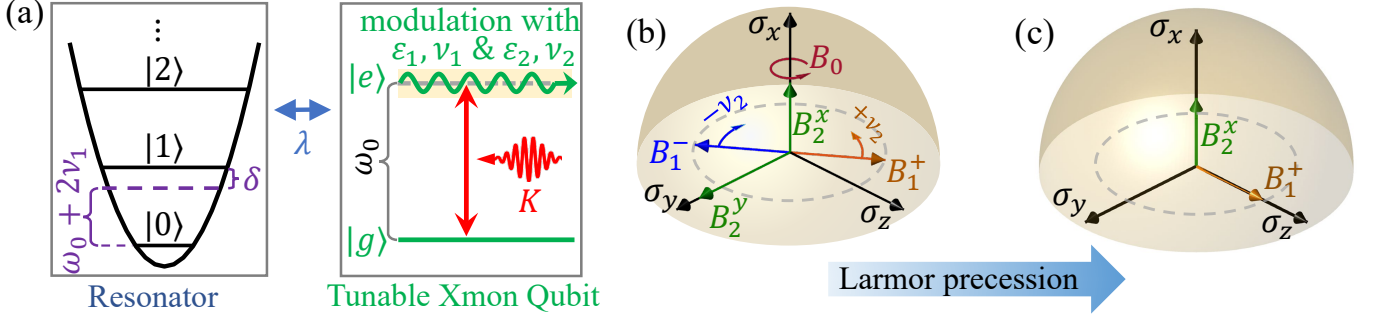


FIG. 1. Theoretical model. (a) Sketch for the qubit-resonator coupling. The test qubit is coupled to the resonator at the second sideband of a sine longitudinal modulation with modulating amplitude  $\varepsilon_1$  and frequency  $\nu_1$ . A second sine modulation with amplitude  $\varepsilon_2$  and frequency  $\nu_2$  is used to control the effective frequency of the qubit. These two modulations, together with a transverse drive  $K$ , effectively realizes an effective Rabi Hamiltonian. Bloch representations in (b) the laboratory frame and (c) the precessing frame. By analogy with the motion of a spin-1/2, the transverse drive can be regarded as a static magnetic field of strength  $B_0 \propto K$  along the  $x$ -axis, which forces the Bloch vector of the qubit to precess with angular frequency  $B_0$ . The second longitudinal modulation corresponds to applying two magnetic fields on the  $yz$ -plane with the same amplitude  $|B_1^\pm| = \varepsilon_2/4$ , rotating at the same angular frequency  $\nu_2 = B_0$ , but in opposite directions. The light field stored in the resonator acts as an effective magnetic field with components  $B_2^x$  and  $B_2^y$ . In the precessing frame associated with  $B_0$ , the components  $B_1^+$  and  $B_2^x$  are aligned with the  $z$ - and  $x$ -axes, respectively. The remaining components have negligible effects in the rotating-wave approximation (not shown).

decoupled from the resonator since the detuning between the qubit and the resonator is twenty times their coupling strength without modulations. Subsequently, an ancilla qubit is tuned on resonance with the resonator, undergoing photon-number-dependent Rabi oscillations. The photonic populations of the resonator can be inferred from the measured Rabi oscillations signals [53]. Figure 2 shows the measured average photon number ( $\bar{n} = \langle a^\dagger a \rangle$ ) versus time. We compare the measured values with the theoretical predictions and show that the experimental result agrees well with the simulation.

The exotic behavior in the SP can be characterized by the Wigner function matrix that contains full information about the joint qubit-resonator state [54]. In terms of the qubit basis  $\{|g\rangle, |e\rangle\}$ , the density operator is expressed as

$$\rho = \sum_{k=g,e} \sum_{k'=g,e} \rho_{k,k'} \otimes |k\rangle\langle k'|, \quad (5)$$

with  $\rho_{k,k'} = \langle k|\rho|k'\rangle$  matrix elements.

The information of the element  $\rho_{k,k'}$  is contained in the corresponding Wigner matrix element  $W_{k,k'}(\beta)$ . To measure the Wigner matrix elements, we translate in phase space the resonator state by  $\beta$ . The matrix elements are inferred by measuring the test qubits along three mutual axes, and correlating the outcomes to the photon number distributions of the resonator measured with the ancilla qubit (see Supplementary Material Sec. S5 [38] for detailed characterization of the qubit-resonator state). Figures 3(a–d) show the Wigner matrix elements reconstructed at  $t = 1.946 \mu\text{s}$ , which reveal that the field exhibits two quasi-classical components with the same amplitude but opposite phases  $|\pm\alpha\rangle$  and a vacuum component, featuring a first-order phase transition. The strong quantum coherence between the “empty” state  $|0\rangle$  and “filled” states  $|\pm\alpha\rangle$ , distinguishes this SPT from the first-order phase transition previously investigated in the Dicke model with the

mean field description [15, 33, 55]. The resulting output state can be regarded as a super-cat state, featuring being simultaneously “empty” and “filled”, where the “filled” state itself is a cat state composed of the two components  $|\pm\alpha\rangle$  superimposed with each other. This super-cat state is significantly distinct from the ground state of the ideal Rabi model with an infinite frequency ratio [18], in which the population of the vacuum component tends to 0. As shown in Fig. S7 of the Supplementary Material [38] Sec. S4, the limitation of the effective frequency ratio, non-adiabaticity, and deviation from model Hamiltonian contribute vacuum populations of 0.04, 0.03, 0.06, respectively. The dissipation is responsible for the rest of vacuum population ( $\sim 0.16$ ), and turns the qubit-resonator system into a partially mixed state, with a purity of  $\text{Tr}(\rho^2) = 0.46$ . With the increase of the distance from the critical point, the size of the cat state would be improved at the price of degradation of the state purity, as a consequence of its increasing sensitivity to dissipation and the longer time needed for the quenching process.

To further confirm this exotic phenomenon, we separate the measured coherent fields with amplitude  $|\alpha|$  from the vacuum field, enabled by their large distance in phase space. The extracted Wigner matrix elements for the SP are displayed in Figs. 3(e–h). As expected, each of these elements exhibits two peaks, between which there exists an oscillating pattern featuring the alternating appearance of positive and negative values, as a consequence of quantum interference between  $|\pm\alpha\rangle$  [56]. The distortions of the Gaussian peaks are mainly due to the neglected high-order nonlinear processes and the limited frequency ratio  $\Omega/\delta \simeq 10$ . These results unambiguously demonstrate that the photons produced in the SP spontaneously form a cat-like state. For each of the two quasiclassical components forming the cat state, the parity symmetry is broken. The extent of the symmetry breaking is quantified

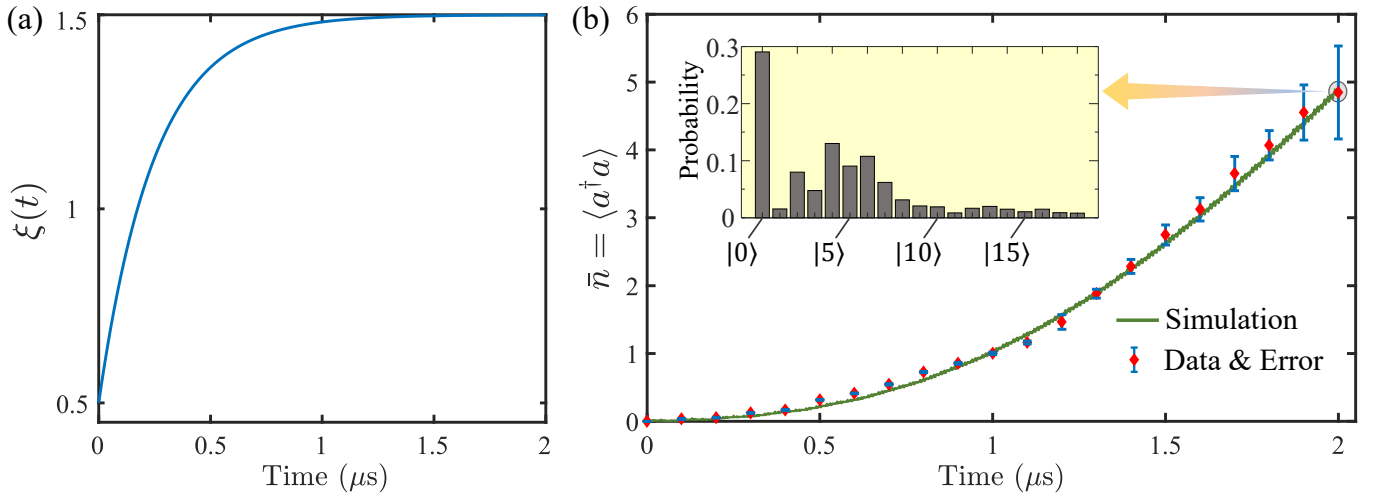


FIG. 2. (a) Control parameter  $\xi(t)$  versus time  $t$ . During the quenching process, the effective frequencies of the qubit and the resonator are respectively varied as  $\Omega = 2\sqrt{10}\eta/[1.5 - \exp(-8t/t_f)]$  and  $\delta \simeq \Omega/10$ , with  $t_f = 2 \mu\text{s}$ , while the effective coupling strength is fixed to  $\eta/2\pi = 0.81$  MHz. Experimentally,  $\Omega$  is controllable by  $\varepsilon_2$ , and  $\delta$  is adjustable by the Stark shift produced by an ancilla qubit dispersively coupled to the resonator. With these settings,  $\xi(t)$  depends on  $t$  as  $\xi(t) = 1.5 - \exp(-8t/t_f)$ . (b) Observed dynamical evolution of the average photon number  $\bar{n} = \langle a^\dagger a \rangle$ . The green curve shows the result of numerical simulation based on the master equation, where the parameters of the control fields are set to:  $K/(2\pi) = 19.9$  MHz,  $\varepsilon_1/(2\pi) = 165.85$  MHz,  $\nu_1/(2\pi) = 200$  MHz,  $\varepsilon_2 = 3.08 \Omega$ ,  $\nu_2/(2\pi) = 33.28$  MHz, and the qubit and resonator frequencies are  $\omega_0/(2\pi) = 5.18$  GHz and  $\omega_p = \omega_0 + 2\nu_1 + \delta$ , respectively. The relaxation time  $T_1$  (dephasing time  $T_2^*$ ) for the qubit and the resonator are  $21.5 \mu\text{s}$  and  $12.9 \mu\text{s}$  ( $1.1 \mu\text{s}$  and  $234.5 \mu\text{s}$ ), respectively, each measured in independent experiments. The inset shows the photon number distribution of the resonator measured at  $t = 2 \mu\text{s}$ .

by the field coherence,  $\langle a \rangle$ , which is equal to the amplitude of the quasiclassical coherent state and can be used as an order parameter to characterize the QPT [18, 57].

After the quenching dynamics, this coherence has a magnitude of 2.62, which indicates the occurrence of a phase transition during the quenching process [58]. The resulting cat state formed by two coherent states  $|\pm\alpha\rangle$  has a size of  $d_-^2 = 4|\alpha|^2 = 27.46$  [56]. The inferred diagonal element  $\mathcal{W}_{e,e}$  ( $\mathcal{W}_{g,g}$ ) has a minimum value of  $-0.060$  ( $-0.068$ ) at  $\beta = -0.48 - 0.36i$  ( $\beta = -0.48i$ ). These negative phase-space quasi-probability densities show the nonclassicality of the emergent photonic field. The photon-matter entanglement can be quantified by using the negativity obtained from the partially transposed density matrix [59]. The negativity for the SP, inferred from the qubit-resonator density matrix associated with the SP, is 0.12, which confirms the existence of strong light-matter entanglement, making the present SP distinct from those realized in previous experiments [9–16], where no entanglement was observed due to the strong decoherence. Because of the decoherence effects, this negativity is smaller than that for the ideal superradiant ground state, which has a value of 0.44.

The quantum coherence between the coexisting phases can be further confirmed by the off-diagonal elements between  $|0\rangle$  and  $|n\rangle$  ( $n \neq 0$ ) in the Fock basis associated with  $\mathcal{W}_{e,e}$  and  $\mathcal{W}_{g,g}$ , displayed in Figs. 3(i) and (j). The coherences between the empty state and filled state, defined as  $\mathcal{C}_{k,k} = \sum_{n \neq 0} |\langle 0|\rho_{k,k}|n\rangle|/\text{Tr}(\rho_{k,k})$ , are 1.018 and 1.020 for the renormalized resonator density matrices correlated

with  $|e\rangle$  and  $|g\rangle$ , respectively. Each of these coherences is much larger than that of the coherent state  $|\alpha\rangle$ ,  $\mathcal{C}_\alpha = \sum_{n \neq 0} |\langle 0|\alpha\rangle\langle\alpha|n\rangle| = 0.1147$ , which verifies that these coherences are mainly due to the quantum superposition between the SP and the normal phase. The negativity of the realized first-order phase transition is 0.25, which quantifies the qubit-resonator of the output density matrix, reconstructed without removing the elements associated with the vacuum state component  $|0\rangle$ . This negativity is significantly higher than that for the SP, mainly due to the fact that the vacuum state is not subjected to decoherence.

In conclusion, we have theoretically proposed and experimentally demonstrated a method for exploring the SPT of a microwave photonic field stored in a resonator coupled to a superconducting artificial atom. The reconstructed resonator-qubit Wigner matrix reveals quantum interference effects between the vacuum and the SP cat states, and between the two SP states, as well as light-matter entanglement. It is expected that the emergent cat state loses its coherence at an increasing rate with the increase of the photon number, as a consequence of the information acquisition about the phase or amplitude of the field by the environment. Progressively increasing the quench parameter would make it possible to experimentally explore the intimate relation between the symmetry breaking process and decoherence, which plays a central role in the quantum-to-classical transition. In addition to fundamental interest, our system may find applications in quantum technology.

We acknowledge helpful discussions with Anton Frisk



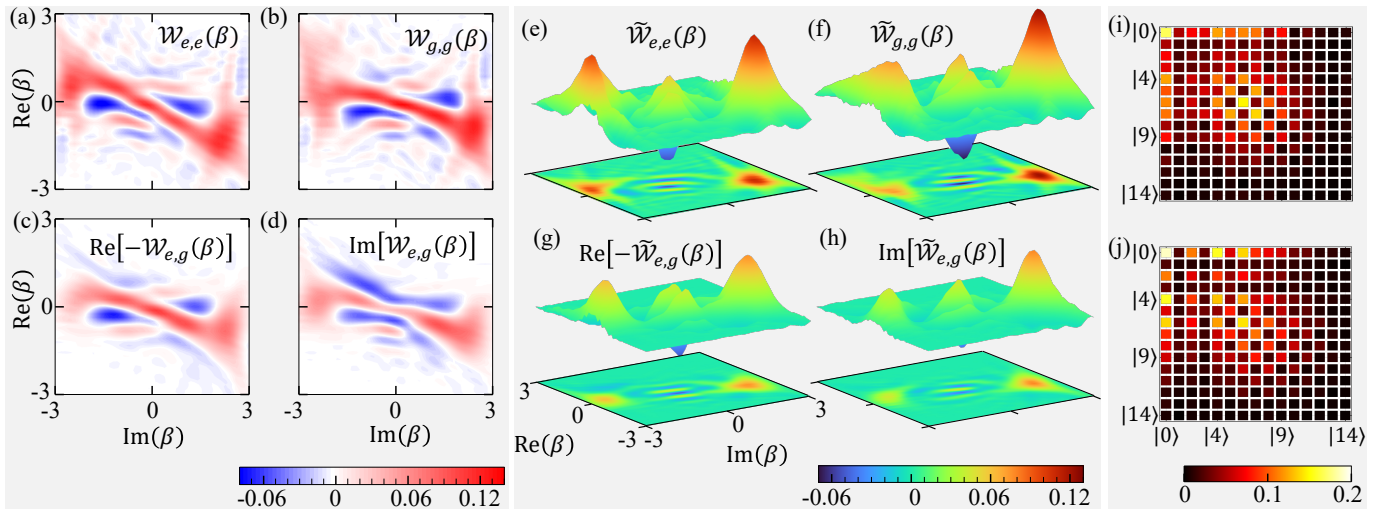


FIG. 3. Wigner matrix tomography. (a–d) Measured matrix elements for the super-cat state. The value of the matrix elements at each point is reconstructed from the Wigner diagonal elements measured along the three mutually orthogonal axes of the Bloch sphere of the qubit. Each of these diagonal elements is obtained from the measured photon number distribution of the field displaced by  $\beta$  in phase space, correlated with detection of the test qubit along the corresponding axis. All the data are measured at  $t = 1.946 \mu\text{s}$ . (e–h) Matrix elements for the superradiant-phase cat state. These Wigner matrix elements are extracted by reconstructing the qubit-resonator density matrix in the Fock basis, discarding the elements associated with  $|0\rangle$  to obtain system density matrix associated with the superradiant phase, from which the corresponding Wigner matrix is obtained. The inferred vacuum population in the superradiant phase is  $\sim 0.1\%$ , which implies that the measured vacuum population of about 30% mainly arises from the normal phase that coexists with the superradiant phase. (i, j) Normalized density matrices of the resonator associated with the qubit states  $|e\rangle$  and  $|g\rangle$ . For clarity, we here only display the magnitudes of the elements.

Kockum. This work was supported by the National Natural Science Foundation of China (Grants No. 12274080, No. 11875108, No. 11934018, No. 11904393, No. 92065114, and No. T2121001), Innovation Program for Quantum Science and Technology under Grant No. 2021ZD0300200, the Strategic Priority Research Program of Chinese Academy of Sciences (Grant No. XDB28000000), the Key-Area Research and Development Program of Guangdong Province, China (Grant No. 2020B0303030001), the Natural Science Funds for Distinguished Young Scholar of Fujian Province under Grant No. 2020J06011, Projects from Fuzhou University under Grants No. JG202001-2 and No. 049050011050, and Beijing Natural Science Foundation (Grant No. Z200009). A.M. is supported by the Polish National Science Centre (NCN) under the Maestro Grant No. DEC-2019/34/A/ST2/00081. F.N. is supported in part by: Nippon Telegraph and Telephone Corporation (NTT) Research, the Japan Science and Technology Agency (JST) [via the Quantum Leap Flagship Program (Q-LEAP), and the Moonshot R&D Grant No. JP-MJMS2061], the Asian Office of Aerospace Research and Development (AOARD) (via Grant No. FA2386-20-1-4069), and the Foundational Questions Institute Fund (FQXi) via Grant No. FQXi-IAF19-06.

\* These authors contribute equally to this work.

† [zbyang@fzu.edu.cn](mailto:zbyang@fzu.edu.cn)

‡ [fnori@riken.jp](mailto:fnori@riken.jp)

§ [t96034@fzu.edu.cn](mailto:t96034@fzu.edu.cn)

- [1] R. H. Dicke, Coherence in spontaneous radiation processes, *Phys. Rev.* **93**, 99 (1954).
- [2] P. Kirton, M. M. Roses, J. Keeling, and E. G. Dalla Torre, Introduction to the Dicke model: From equilibrium to nonequilibrium, and vice versa, *Adv. Quantum Technol.* **2**, 1800043 (2019).
- [3] Y. K. Wang and F. T. Hioe, Phase transition in the Dicke model of superradiance, *Phys. Rev. A* **7**, 831 (1973).
- [4] K. Hepp and E. H. Lieb, On the superradiant phase transition for molecules in a quantized radiation field: the Dicke maser model, *Ann. Phys.* **76**, 360 (1973).
- [5] N. Lambert, C. Emary, and T. Brandes, Entanglement and the phase transition in single-mode superradiance, *Phys. Rev. Lett.* **92**, 073602 (2004).
- [6] P. Nataf and C. Ciuti, Protected quantum computation with multiple resonators in ultrastrong coupling circuit QED, *Phys. Rev. Lett.* **107**, 190402 (2011).
- [7] H. Kwon, K. C. Tan, T. Volkoff, and H. Jeong, Nonclassicality as a quantifiable resource for quantum metrology, *Phys. Rev. Lett.* **122**, 040503 (2019).
- [8] K. Rzażewski, K. Wódkiewicz, and W. Żakowicz, Phase transitions, two-level atoms, and the  $A^2$  term, *Phys. Rev. Lett.* **35**, 432 (1975).
- [9] Z. Zhang, C. H. Lee, R. Kumar, K. J. Arnold, S. J. Masson, A. S. Parkins, and M. D. Barrett, Nonequilibrium phase transition in a spin-1 Dicke model, *Optica* **4**, 424 (2017).
- [10] K. Baumann, C. Guerlin, F. Brennecke, and T. Esslinger, Dicke quantum phase transition with a superfluid gas in an optical cavity, *Nature* **464**, 1301 (2010).
- [11] K. Baumann, R. Mottl, F. Brennecke, and T. Esslinger, Exploring symmetry breaking at the Dicke quantum phase transition, *Phys. Rev. Lett.* **107**, 140402 (2011).

- [12] F. Brennecke, R. Mottl, K. Baumann, R. Landig, T. Donner, and T. Esslinger, Real-time observation of fluctuations at the driven-dissipative Dicke phase transition, *Proc. Nat. Acad. Sci.* **110**, 11763 (2013).
- [13] J. Klinder, H. Keßler, M. Wolke, L. Mathey, and A. Hemmerich, Dynamical phase transition in the open Dicke model, *Proc. Nat. Acad. Sci.* **112**, 3290 (2015).
- [14] J. Léonard, A. Morales, P. Zupancic, T. Esslinger, and T. Donner, Supersolid formation in a quantum gas breaking a continuous translational symmetry, *Nature* **543**, 87 (2017).
- [15] F. Ferri, R. Rosa-Medina, F. Finger, N. Dogra, M. Soriente, O. Zilberberg, T. Donner, and T. Esslinger, Emerging dissipative phases in a superradiant quantum gas with tunable decay, *Phys. Rev. X* **11**, 041046 (2021).
- [16] X. Zhang, Y. Chen, Z. Wu, J. Wang, J. Fan, S. Deng, and H. Wu, Observation of a superradiant quantum phase transition in an intracavity degenerate Fermi gas, *Science* **373**, 1359 (2021).
- [17] S. Ashhab, Superradiance transition in a system with a single qubit and a single oscillator, *Phys. Rev. A* **87**, 013826 (2013).
- [18] M.-J. Hwang, R. Puebla, and M. B. Plenio, Quantum phase transition and universal dynamics in the Rabi model, *Phys. Rev. Lett.* **115**, 180404 (2015).
- [19] D. Lv, S. An, Z. Liu, J.-N. Zhang, J. S. Pedernales, L. Lamata, E. Solano, and K. Kim, Quantum simulation of the quantum Rabi model in a trapped ion, *Phys. Rev. X* **8**, 021027 (2018).
- [20] M.-L. Cai, Z.-D. Liu, W.-D. Zhao, Y.-K. Wu, Q.-X. Mei, Y. Jiang, L. He, X. Zhang, Z.-C. Zhou, and L.-M. Duan, Observation of a quantum phase transition in the quantum Rabi model with a single trapped ion, *Nat. Commun.* **12**, 1126 (2021).
- [21] A. F. Kockum, A. Miranowicz, S. D. Liberato, S. Savasta, and F. Nori, Ultrastrong coupling between light and matter, *Nat. Rev. Phys.* **1**, 19 (2019).
- [22] P. Forn-Díaz, L. Lamata, E. Rico, J. Kono, and E. Solano, Ultrastrong coupling regimes of light-matter interaction, *Rev. Mod. Phys.* **91**, 025005 (2019).
- [23] X. Gu, A. F. Kockum, A. Miranowicz, Y.-X. Liu, and F. Nori, Microwave photonics with superconducting quantum circuits, *Phys. Rep.* **718-719**, 1 (2017).
- [24] D. Ballester, G. Romero, J. J. García-Ripoll, F. Deppe, and E. Solano, Quantum simulation of the ultrastrong-coupling dynamics in circuit quantum electrodynamics, *Phys. Rev. X* **2**, 021007 (2012).
- [25] M. Feng, Y. P. Zhong, T. Liu, L. L. Yan, W. L. Yang, J. Twamley, and H. Wang, Exploring the quantum critical behaviour in a driven Tavis-Cummings circuit, *Nat. Commun.* **6**, 7111 (2015).
- [26] K. Xu, Z.-H. Sun, W. Liu, Y.-R. Zhang, H. Li, H. Dong, W. Ren, P. Zhang, F. Nori, D. Zheng, H. Fan, and H. Wang, Probing dynamical phase transitions with a superconducting quantum simulator, *Sci. Adv.* **6**, eaba4935 (2020).
- [27] F. Yoshihara, T. Fuse, Z. Ao, S. Ashhab, K. Kakuyanagi, S. Saito, T. Aoki, K. Koshino, and K. Semba, Inversion of qubit energy levels in qubit-oscillator circuits in the deep-strong-coupling regime, *Phys. Rev. Lett.* **120**, 183601 (2018).
- [28] P. Nataf and C. Ciuti, No-go theorem for superradiant quantum phase transitions in cavity QED and counter-example in circuit QED, *Nat. Commun.* **1**, 72 (2010).
- [29] D. De Bernardis, P. Pilar, T. Jaako, S. De Liberato, and P. Rabl, Breakdown of gauge invariance in ultrastrong-coupling cavity QED, *Phys. Rev. A* **98**, 053819 (2018).
- [30] C. Sánchez Muñoz, A. Frisk Kockum, A. Miranowicz, and F. Nori, Simulating ultrastrong-coupling processes breaking parity conservation in Jaynes-Cummings systems, *Phys. Rev. A* **102**, 033716 (2020).
- [31] W. Qin, A. Miranowicz, P.-B. Li, X.-Y. Lü, J. Q. You, and F. Nori, Exponentially enhanced light-matter interaction, cooperativities, and steady-state entanglement using parametric amplification, *Phys. Rev. Lett.* **120**, 093601 (2018).
- [32] C. Leroux, L. C. G. Govia, and A. A. Clerk, Enhancing cavity quantum electrodynamics via antisqueezing: Synthetic ultrastrong coupling, *Phys. Rev. Lett.* **120**, 093602 (2018).
- [33] C. J. Zhu, L. L. Ping, Y. P. Yang, and G. S. Agarwal, Squeezed light induced symmetry breaking superradiant phase transition, *Phys. Rev. Lett.* **124**, 073602 (2020).
- [34] Y.-H. Chen, W. Qin, X. Wang, A. Miranowicz, and F. Nori, Shortcuts to adiabaticity for the quantum Rabi model: Efficient generation of giant entangled cat states via parametric amplification, *Phys. Rev. Lett.* **126**, 023602 (2021).
- [35] N. K. Langford, R. Sagastizabal, M. Kounalakis, C. Dickel, A. Bruno, F. Luthi, D. J. Thoen, A. Endo, and L. DiCarlo, Experimentally simulating the dynamics of quantum light and matter at deep-strong coupling, *Nat. Commun.* **8**, 1715 (2017).
- [36] J. Braumüller, M. Marthaler, A. Schneider, A. Stehli, H. Rotzinger, M. Weides, and A. V. Ustinov, Analog quantum simulation of the Rabi model in the ultra-strong coupling regime, *Nat. Commun.* **8**, 779 (2017).
- [37] D.-W. Wang, C. Song, W. Feng, H. Cai, D. Xu, H. Deng, H. Li, D. Zheng, X. Zhu, H. Wang, S.-Y. Zhu, and M. O. Scully, Synthesis of antisymmetric spin exchange interaction and chiral spin clusters in superconducting circuits, *Nat. Phys.* **15**, 382 (2019).
- [38] See Supplemental Material for a derivation of the effective Rabi Hamiltonian, a description of the system parameters, experimental pulse sequences, quenching dynamics, and techniques for characterizing the qubit-resonator output states, a discussion of experimental imperfections, including the limitation of the effective frequency ratio, non-adiabaticity, dissipation, and deviations from the ideal Hamiltonian, as well as a numerical simulation of the superradiant phase transition in the Dicke model, which includes Refs. [39-51].
- [39] C. Song, S.-B. Zheng, P. Zhang, K. Xu, L. Zhang, Q. Guo, W. Liu, D. Xu, H. Deng, K. Huang, D. Zheng, X. Zhu, and H. Wang, Continuous-variable geometric phase and its manipulation for quantum computation in a superconducting circuit, *Nat. Commun.* **8**, 1061 (2017).
- [40] W. Ning, X.-J. Huang, P.-R. Han, H. Li, H. Deng, Z.-B. Yang, Z.-R. Zhong, Y. Xia, K. Xu, D. Zheng, and S.-B. Zheng, Deterministic entanglement swapping in a superconducting circuit, *Phys. Rev. Lett.* **123**, 060502 (2019).
- [41] C. Song, K. Xu, W. Liu, C.-p. Yang, S.-B. Zheng, H. Deng, Q. Xie, K. Huang, Q. Guo, L. Zhang, P. Zhang, D. Xu, D. Zheng, X. Zhu, H. Wang, Y.-A. Chen, C.-Y. Lu, S. Han, and J.-W. Pan, 10-qubit entanglement and parallel logic operations with a superconducting circuit, *Phys. Rev. Lett.* **119**, 180511 (2017).
- [42] Q.-X. Mei, B.-W. Li, Y.-K. Wu, M.-L. Cai, Y. Wang, L. Yao, Z.-C. Zhou, and L.-M. Duan, Experimental realization of the Rabi-Hubbard model with trapped ions, *Phys. Rev. Lett.* **128**, 160504 (2022).
- [43] D. M. Meekhof, C. Monroe, B. E. King, W. M. Itano, and D. J. Wineland, Generation of nonclassical motional states of a trapped atom, *Phys. Rev. Lett.* **76**, 1796 (1996).
- [44] D. Leibfried, R. Blatt, C. Monroe, and D. Wineland, Quantum dynamics of single trapped ions, *Rev. Mod. Phys.* **75**, 281 (2003).
- [45] D. Lv, S. An, Z. Liu, J.-N. Zhang, J. S. Pedernales, L. Lamata, E. Solano, and K. Kim, Quantum simulation of the quantum Rabi model in a trapped ion, *Phys. Rev. X* **8**, 021027 (2018).

- [46] M. Grant and S. Boyd, Cvx: Matlab software for disciplined convex programming, version 2.0 beta. <http://cvxr.com/cvx>, (2013).
- [47] G. Vidal and R. F. Werner, Computable measure of entanglement, *Phys. Rev. A* **65**, 032314 (2002).
- [48] W. P. Schleich, [Quantum Optics in Phase Space](#) (Wiley, Berlin, 2001).
- [49] M. Tavis and F. W. Cummings, Exact solution for an  $N$ -molecule-radiation-field Hamiltonian, *Phys. Rev.* **170**, 379 (1968).
- [50] C. Song, K. Xu, H. Li, Y.-R. Zhang, X. Zhang, W. Liu, Q. Guo, Z. Wang, W. Ren, J. Hao, H. Feng, H. Fan, D. Zheng, D.-W. Wang, H. Wang, and S.-Y. Zhu, Generation of multicomponent atomic Schrödinger cat states of up to 20 qubits, *Science* **365**, 574 (2019).
- [51] C. Emary and T. Brandes, Quantum chaos triggered by precursors of a quantum phase transition: The Dicke model, *Phys. Rev. Lett.* **90**, 044101 (2003).
- [52] R. Gutiérrez-Jáuregui and G. S. Agarwal, Probing the spectrum of the Jaynes-Cummings-Rabi model by its isomorphism to an atom inside a parametric amplifier cavity, *Phys. Rev. A* **103**, 023714 (2021).
- [53] M. Hofheinz, H. Wang, M. Ansmann, R. C. Bialczak, E. Lucero, M. Neeley, A. D. O’Connell, D. Sank, J. Wenner, J. M. Martinis, and A. N. Cleland, Synthesizing arbitrary quantum states in a superconducting resonator, *Nature* **459**, 546 (2009).
- [54] S. Wallentowitz, R. L. de Matos Filho, and W. Vogel, Determination of entangled quantum states of a trapped atom, *Phys. Rev. A* **56**, 1205 (1997).
- [55] M. Soriente, T. Donner, R. Chitra, and O. Zilberberg, Dissipation-induced anomalous multicritical phenomena, *Phys. Rev. Lett.* **120**, 183603 (2018).
- [56] S. Deléglise, I. Dotsenko, C. Sayrin, J. Bernu, M. Brune, J.-M. Raimond, and S. Haroche, Reconstruction of non-classical cavity field states with snapshots of their decoherence, *Nature* **455**, 510 (2008).
- [57] M.-J. Hwang and M. B. Plenio, Quantum phase transition in the finite Jaynes-Cummings lattice systems, *Phys. Rev. Lett.* **117**, 123602 (2016).
- [58] S. Sachdev, [Quantum Phase Transitions](#), 2nd ed. (Cambridge University Press, 2011).
- [59] R. Horodecki, P. Horodecki, M. Horodecki, and K. Horodecki, Quantum entanglement, *Rev. Mod. Phys.* **81**, 865 (2009).

# Supplemental Material for “Observation of a superradiant phase transition with emergent cat states”

Ri-Hua Zheng,<sup>1,\*</sup> Wen Ning,<sup>1,\*</sup> Ye-Hong Chen,<sup>1,2,3,\*</sup> Jia-Hao Lü,<sup>1</sup> Li-Tuo Shen,<sup>1</sup> Kai Xu,<sup>4,5</sup> Yu-Ran Zhang,<sup>6,2,3</sup> Da Xu,<sup>7</sup> Hekang Li,<sup>5</sup> Yan Xia,<sup>1</sup> Fan Wu,<sup>1</sup> Zhen-Biao Yang,<sup>1,†</sup> Adam Miranowicz,<sup>2,8</sup> Neill Lambert,<sup>2</sup> Dongning Zheng,<sup>4,5</sup> Heng Fan,<sup>4,5</sup> Franco Nori,<sup>2,3,9,‡</sup> and Shi-Biao Zheng<sup>1,§</sup>

<sup>1</sup>*Fujian Key Laboratory of Quantum Information and Quantum Optics,  
College of Physics and Information Engineering,  
Fuzhou University, Fuzhou, Fujian 350108, China*

<sup>2</sup>*Theoretical Quantum Physics Laboratory, RIKEN Cluster for Pioneering Research, Wako-shi, Saitama 351-0198, Japan*

<sup>3</sup>*Quantum Information Physics Theory Research Team,  
RIKEN Center for Quantum Computing (RQC), Wako-shi, Saitama 351-0198, Japan*

<sup>4</sup>*Institute of Physics and Beijing National Laboratory for Condensed Matter Physics,  
Chinese Academy of Sciences, Beijing 100190, China*

<sup>5</sup>*CAS Center for Excellence in Topological Quantum Computation,  
University of Chinese Academy of Sciences, Beijing 100190, China*

<sup>6</sup>*School of Physics and Optoelectronics, South China University of Technology, Guangzhou 510640, China*

<sup>7</sup>*Interdisciplinary Center of Quantum Information,  
State Key Laboratory of Modern Optical Instrumentation and  
Zhejiang Province Key Laboratory of Quantum Technology and Device,  
School of Physics, Zhejiang University, Hangzhou 310027, China*

<sup>8</sup>*Institute of Spintronics and Quantum Information, Faculty of Physics,  
Adam Mickiewicz University, 61-614 Poznań, Poland*

<sup>9</sup>*Department of Physics, University of Michigan, Ann Arbor, Michigan 48109-1040, USA*

## Contents

<b>S1. Effective quantum Rabi model</b>	3
A. Derivation of the effective quantum Rabi Hamiltonian	3
B. Superradiant phase transition under ideal conditions	4
<b>S2. Experimental setup, device parameters, and pulse sequence</b>	5
<b>S3. Control of quenching dynamics</b>	7
A. Time-dependence of the normalized coupling parameter $\xi$	7
B. Control of the effective qubit frequency $\Omega$	8
C. Control of the effective resonator frequency $\delta$	8
<b>S4. Effects of off-resonant couplings and decoherence</b>	10
<b>S5. Characterization of the qubit-resonator state</b>	12
A. Photon-number distribution	12
B. Diagonal Wigner matrix elements	13
C. Off-diagonal Wigner matrix elements	15
<b>S6. Measure of the qubit-resonator entanglement</b>	16
<b>S7. Characterization of the super-cat state</b>	17
<b>S8. Numerical simulation of the Dicke-model SPT</b>	17

---

\*These authors contribute equally to this work.

†Electronic address: [zbyang@fzu.edu.cn](mailto:zbyang@fzu.edu.cn)

‡Electronic address: [fnori@riken.jp](mailto:fnori@riken.jp)

§Electronic address: [t96034@fzu.edu.cn](mailto:t96034@fzu.edu.cn)



References

## S1. EFFECTIVE QUANTUM RABI MODEL

### A. Derivation of the effective quantum Rabi Hamiltonian

When the drive is tuned to the carrier, the dynamics is described by the Hamiltonian ( $\hbar = 1$  hereafter)

$$H = H_0 + H_I, \quad (\text{S1})$$

where

$$\begin{aligned} H_0 &= (\omega_0 + 2\nu_1) a^\dagger a + \frac{1}{2}[\omega_0 + \varepsilon_1 \cos(\nu_1 t)]\sigma_z, \\ H_I &= \delta a^\dagger a + \frac{1}{2}\varepsilon_2 \cos(\nu_2 t)\sigma_z + (\lambda a^\dagger \sigma_- + K e^{i\omega_0 t} \sigma_- + \text{h.c.}). \end{aligned} \quad (\text{S2})$$

Here,  $\sigma_z = |e\rangle\langle e| - |g\rangle\langle g|$  and  $\sigma_- = |g\rangle\langle e|$  are Pauli operators for the qubit. Performing the transformation

$$U_0 = \exp \left[ i \int_0^t H_0 dt \right], \quad (\text{S3})$$

we obtain the system Hamiltonian in the rotating frame

$$H'_I = \delta a^\dagger a + \frac{1}{2}\varepsilon_2 \cos(\nu_2 t)\sigma_z + \left\{ \exp[-i\mu \sin(\nu_1 t)] [\lambda \exp(2i\nu_1 t) a^\dagger + K] \sigma_- + \text{h.c.} \right\}, \quad (\text{S4})$$

where  $\mu = \varepsilon_1/\nu_1$ . Using the Jacobi-Anger expansion

$$\exp[i\mu \sin(\nu_1 t)] = \sum_{m=-\infty}^{\infty} J_m(\mu) \exp(im\nu_1 t), \quad (\text{S5})$$

with  $J_m(\mu)$  being the  $m$ th Bessel function of the first kind, we obtain

$$H'_I = \delta a^\dagger a + \frac{1}{2}\varepsilon_2 \cos(\nu_2 t)\sigma_z + \left( \sum_{m=-\infty}^{\infty} J_m(\mu) \left\{ \lambda \exp[-i(m-2)\nu_1 t] a^\dagger + K \exp(-im\nu_1 t) \right\} \sigma_- + \text{h.c.} \right). \quad (\text{S6})$$

ADC	Analog-to-Digital Converter
DAC	Digital-to-Analog Converter
DC	Direct Current
HEMT	High Electron Mobility Transistor
IQ	In-phase and Quadrature
JPA	Josephson Parametric Amplifier
MC	Mixing Chamber
MS	Microwave Source
NP	Normal Phase
RC	Resistance Capacitance
RI	Read-In
RO	Read-Out
SPT	Superradiant Phase Transition
SP	Superradiant Phase

TABLE S1: Abbreviations used in this supplemental material.

Assuming that  $\{|\lambda J_2(\mu)|, |K J_0(\mu)|, \delta, \varepsilon_2\} \ll \nu_1$ , we can discard the fast-oscillating terms, thus  $H_I'$  reduces to

$$\begin{aligned} H_I' &= [J_2(\mu)\lambda a^\dagger \sigma_- + K J_0(\mu)\sigma_- + \text{h.c.}] + \delta a^\dagger a + \frac{1}{2}\varepsilon_2 \cos(\nu_2 t)\sigma_z \\ &= \frac{1}{2}B_0\sigma_x + \frac{1}{2}\varepsilon_2 \cos(\nu_2 t)\sigma_z + \delta a^\dagger a + \eta(X\sigma_x - Y\sigma_y), \end{aligned} \quad (\text{S7})$$

where  $B_0 = 2K J_0(\mu)$ ,  $\eta = \lambda J_2(\mu)/2$ ,  $X = a^\dagger + a$ ,  $Y = i(a^\dagger - a)$ ,  $\sigma_x = \sigma_- + \sigma_-^\dagger$ , and  $\sigma_y = i\sigma_- - i\sigma_-^\dagger$ . Under the transformation  $\exp(iB_0\sigma_x t/2)$ , the system Hamiltonian in the moving frame becomes

$$\begin{aligned} H_I'' &= \eta\{X\sigma_x - Y[\cos(B_0 t)\sigma_y - \sin(B_0 t)\sigma_z]\} \\ &\quad + \delta a^\dagger a + \frac{1}{2}\varepsilon_2 \cos(\nu_2 t)[\cos(B_0 t)\sigma_z + \sin(B_0 t)\sigma_y]. \end{aligned} \quad (\text{S8})$$

In the limit of  $B_0 \gg \eta, \varepsilon_2/2$  and  $\nu_2 = B_0$ , the fast-oscillating terms can be neglected, and  $H_I''$  reduces to the Rabi Hamiltonian

$$H_R = \frac{1}{2}\Omega\sigma_z + \delta a^\dagger a + \eta\sigma_x(a^\dagger + a), \quad (\text{S9})$$

where  $\Omega = \varepsilon_2/2$  is the effective qubit frequency.

Some fast-oscillating terms in Eq. (S6) cannot be ignored, and induce additional Stark shifts to the effective qubit- and cavity-frequencies. Detailed discussions about these Stark shifts are shown in Sec. S4.

## B. Superradiant phase transition under ideal conditions

In the limit of  $\Omega/\delta \rightarrow \infty$ , we can diagonalize the Rabi Hamiltonian  $H_R$  using a Schrieffer-Wolff transformation [S1]. After applying a unitary operator

$$U_{\text{SW}} = \exp\left[i\frac{\eta}{\Omega}(a^\dagger + a)\sigma_y\right], \quad (\text{S10})$$

and keeping the terms up to second order in the qubit-resonator coupling strengths, Eq. (S9) becomes

$$H_{\text{np}} = \delta a^\dagger a + \frac{\Omega}{2}\sigma_z + \frac{\delta\xi^2}{4}(a + a^\dagger)^2\sigma_z, \quad (\text{S11})$$

which provides a faithful description of the system ground state in the normal phase (NP) of the model, where  $\xi = 2\eta/\sqrt{\Omega\delta}$  is a normalized coupling parameter. Equation (S11) shows that the ground-qubit-state subspace  $\{|n\rangle|g\rangle\}$  is decoupled from the excited-qubit-state subspace  $\{|n\rangle|e\rangle\}$ . Therefore, upon a projection  $\langle g|H_{\text{np}}|g\rangle$  for  $\xi \leq 1$ , one can solve the ground eigenstate and eigenvalue of  $H_R$  as

$$|\psi_{\text{np}}\rangle = S(r_{\text{np}})|0\rangle|g\rangle, \quad \mathcal{E}_{\text{np}} = \delta\sqrt{1 - \xi^2}, \quad (\text{S12})$$

where  $S(r_{\text{np}}) = \exp[(r_{\text{np}}a^{\dagger 2} - r_{\text{np}}^*a^2)/2]$  is the squeezing operator with a real squeezing parameter  $r_{\text{np}} = -\frac{1}{4}\ln(1 - \xi^2)$ . Thus, the excitation energy  $\mathcal{E}_{\text{np}}$  is a positive real number for  $\xi < 1$  and vanishes at  $\xi = 1$ , i.e., in the NP.

For  $\xi > 1$ , the number of photons occupied in the cavity field becomes proportional to  $\Omega/\delta$  and acquires macroscopic occupations, i.e., in the superradiance phase (SP) [S1]. To capture the physics of the SP, we displace the bosonic mode in the Rabi Hamiltonian  $H_R$ . For a displacement parameter  $\alpha = \sqrt{[\Omega/(4\xi^2\delta)](\xi^4 - 1)}$ , we obtain

$$\begin{aligned} H_R'(\pm\alpha) &= D^\dagger(\pm\alpha)H_R D(\pm\alpha) \\ &= \delta a^\dagger a + \frac{\tilde{\Omega}}{2}\tilde{\sigma}_z^\pm + \tilde{\eta}(a + a^\dagger)\tilde{\sigma}_x^\pm + \delta\alpha^2, \end{aligned} \quad (\text{S13})$$

where  $\tilde{\Omega} = \xi^2 \Omega$ ,  $\tilde{\eta} = \sqrt{\delta \Omega} / (2\xi)$ , and

$$D(\alpha) = \exp(\alpha a^\dagger - \alpha^* a), \quad \tilde{\sigma}_z^\pm = |\uparrow^\pm\rangle\langle\uparrow^\pm| - |\downarrow^\pm\rangle\langle\downarrow^\pm|, \quad \tilde{\sigma}_x^\pm = |\uparrow^\pm\rangle\langle\downarrow^\pm| + |\downarrow^\pm\rangle\langle\uparrow^\pm|. \quad (\text{S14})$$

The states

$$|\uparrow^\pm\rangle = \cos(\theta)|e\rangle \pm \sin(\theta)|g\rangle, \quad |\downarrow^\pm\rangle = \mp \sin(\theta)|e\rangle + \cos(\theta)|g\rangle, \quad (\text{S15})$$

are the eigenstates of the terms  $(\frac{\Omega}{2}\sigma_z \pm 2\alpha\eta\sigma_x)$  that construct a new qubit eigenstate subspace, where  $\theta$  obeys

$$\tan \theta = \sqrt{\frac{\xi^2 - 1}{\xi^2 + 1}}. \quad (\text{S16})$$

Then, employing the same procedure used to derive  $H_{\text{np}}$ , we obtain

$$H_{\text{sp}} = \delta a^\dagger a + \frac{\delta}{4\xi^4} (a^\dagger + a)^2 \tilde{\sigma}_z^\pm + \frac{\Omega}{4} (\xi^2 + \xi^{-2}) \tilde{\sigma}_z^\pm. \quad (\text{S17})$$

Applying the projection  $\langle\downarrow^\pm|H_{\text{sp}}|\downarrow^\pm\rangle$ , Eq. (S17) becomes

$$H_{\text{sp}} = \delta a^\dagger a - \frac{\delta}{4\xi^4} (a^\dagger + a)^2 - \frac{\Omega}{4} (\xi^2 + \xi^{-2}), \quad (\text{S18})$$

whose excitation energy is found to be  $\mathcal{E}_{\text{sp}} = \delta\sqrt{1 - \xi^{-4}}$ . The ground eigenstates of the quantum Rabi Hamiltonian  $H_R$  for  $\xi > 1$  are

$$|\psi_{\text{sp}}\rangle = D(\pm\alpha)S(r_{\text{sp}})|0\rangle|\downarrow^\pm\rangle, \quad (\text{S19})$$

which are degenerate, where  $r_{\text{sp}} = -\frac{1}{4}\ln(1 - \xi^{-4})$ .

Therefore,  $H_{\text{np}}$  and  $H_{\text{sp}}$  are the exact low-energy effective Hamiltonians for the NP ( $\xi < 1$ ) and SP ( $\xi > 1$ ), respectively.

## S2. EXPERIMENTAL SETUP, DEVICE PARAMETERS, AND PULSE SEQUENCE

The whole electronics and wiring for our superconducting circuit control are outlined in Fig. S1 [S2, S3]. The superconducting circuit sample, used in our experiment, possesses a bus resonator and five Xmon qubits. Each qubit has its own read-out resonator for reading out its states. The bus resonator has a fixed bare frequency  $\omega_p/2\pi = 5.581$  GHz and a photonic decay time  $T_{1,p} = 12.9 \mu\text{s}$ . Every qubit has two control lines: an XY-control for flipping its states and a Z-control for modulating its frequency, allowing the qubit to flexibly couple with the bus resonator. This, together with the relatively long lifetime of the resonator photons, guarantees the slow quenching manipulation of the qubit-resonator ground state to induce the appearance of the superradiant phase transition (SPT) accompanied by the sudden birth of a photonic mesoscopic superposition of a considerable size. For clarity, Table S1 lists the abbreviations used in this supplemental material.

The XY-controls on the qubits are implemented through the mixing of the low-frequency signals yielded by the IQ channels of two digital-to-analog converters (DACs) and a microwave source (MS). The carrier frequency of the MS is about 5.5 GHz. The Z-controls on the qubits are implemented by two signals: one is produced by the direct-current (DC) biasing line from a low-frequency DC source; the other comes directly from the Z-control of a DAC. The qubit read-out is realized through mixing the signals of the IQ channels of two DACs and an MS with a frequency  $\sim 6.69$  GHz, which output a read-out pulse with multiple tones targeting all resonators for qubit read-out. The output from the circuit is amplified sequentially by an impedance-transformed Josephson parametric amplifier (JPA), high electron mobility transistor (HEMT), and room temperature amplifiers. Then, it is captured and demodulated by analog-to-digital converters (ADCs). Both DACs and ADCs are supported by a field-programmable gate array which reacts at a nanosecond-level speed. The JPA is pumped by an MS with a frequency  $\sim 13.5$  GHz and modulated by



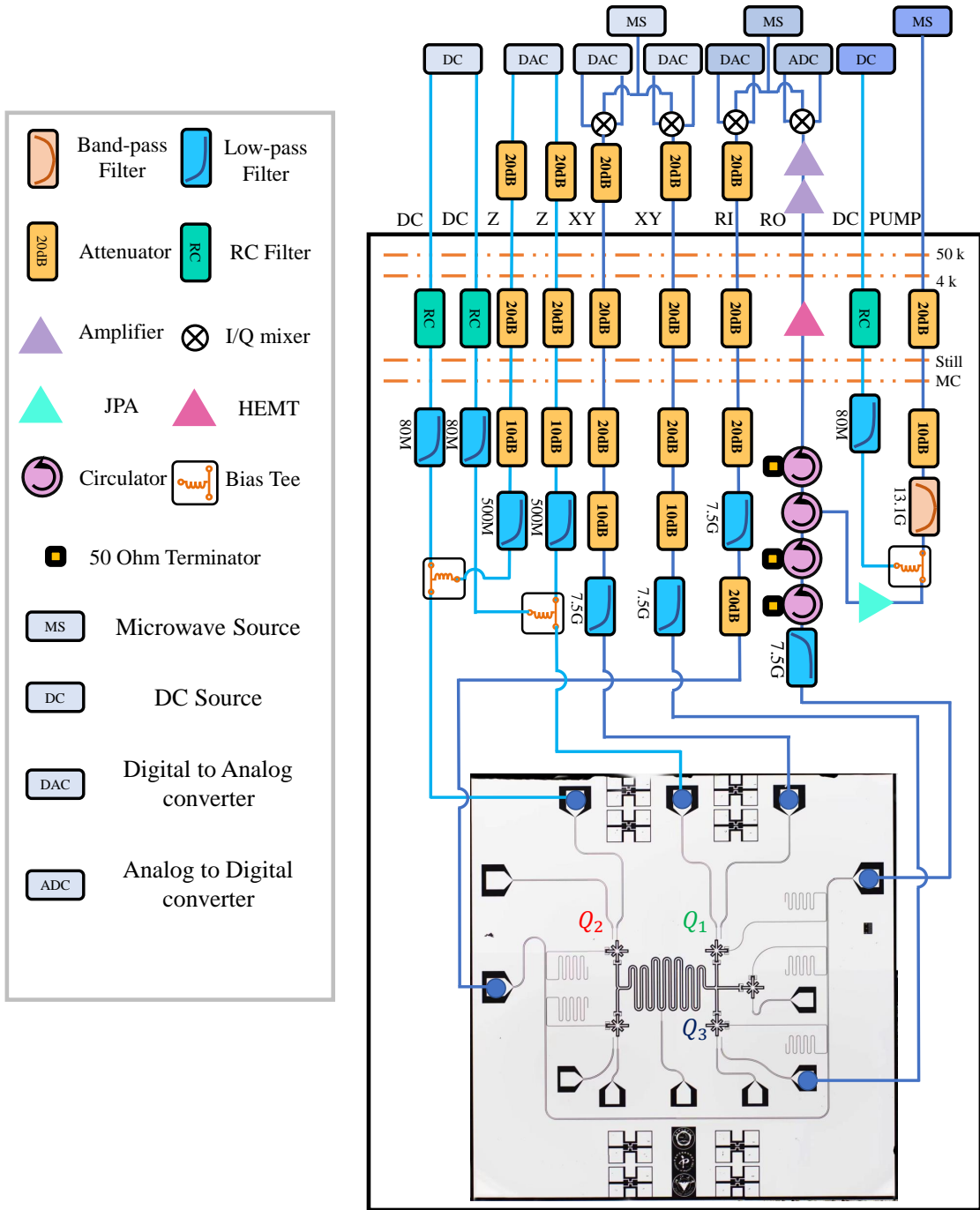


FIG. S1: Schematic diagram of the experimental setup. Note there is a low-pass filter (7.5G) inverted with the others because it connects to the read-out line.

a DC bias. Moreover, some circulators, attenuators, and filters are added to the signal lines in specific temperature regions to reduce the noises that influence the performance of the device.

Three of the five qubits are used in our experiment. One is used as the test qubit  $Q_1$  for realizing the effective quantum Rabi model. The second one acts as an ancilla qubit  $Q_2$  to determine the photon-number distribution for analyzing the Wigner function distribution whose negativity reveals and quantifies the nonclassicality of the light field. The XY-line of the third qubit  $Q_3$  is used to control the bus resonator (by cross-talk interactions) for performing a displacement operation on its states in phase space.

The performance characterization of the qubits and the resonator are listed in Table S2. For technical details about

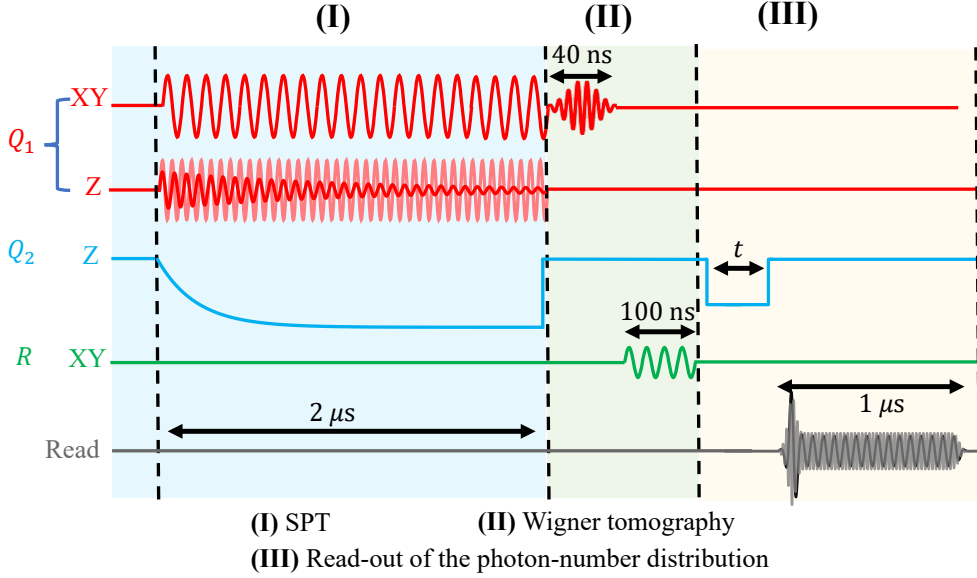


FIG. S2: Sketch of the pulse sequences, which consists of three steps: (I) superradiant phase transition (SPT); (II) Wigner tomography; and (III) read-out of the photon-number distribution. In (I), we apply a continuous drive pulse (amplitude  $K/2\pi = 19.91$  MHz and frequency  $\omega_0/2\pi = 5.18$  GHz) to the XY-line and two tunable pulses  $[\varepsilon_1 \cos(\mu_1 t)$  and  $\varepsilon_2 \cos(\mu_2 t)$ , with  $\{\varepsilon_1, \nu_1, \nu_2\}/2\pi = \{165.85, 200, 33.28\}$  MHz] to the Z-line of the test qubit  $Q_1$ , where the amplitude of the second modulation pulse,  $\varepsilon_2$ , slowly decreases with time, corresponding to the decrease of  $\Omega(t)$ . Moreover, the frequency  $f(t)$  of the ancilla qubit  $Q_2$  decreases with the amplitude of the Z-line, inducing a decrease in the  $\delta(t)$  by Stark shifts. In (II) a single-qubit rotation operation [the identity operation,  $R_x(\pi/2)$ , or  $R_y(\pi/2)$ ] is applied to the test qubit, and a displacement operation  $D(-\beta)$  is then applied to the resonator (actually by tuning the XY-line of  $Q_3$  with cross-talk interactions, not shown). In (III) the ancilla qubit  $Q_2$  is resonantly coupled to the resonator for a given time  $\tau$ , and then biased to its idle frequency ( $f_{\text{idle}}/2\pi = 5.93$  GHz) for state read-out.

	$\omega_{10}/2\pi$ (GHz)	$T_1$ ( $\mu\text{s}$ )	$T_2^*$ ( $\mu\text{s}$ )	$T_2^{\text{SE}}$ ( $\mu\text{s}$ )	$\lambda/2\pi$ (MHz)	$\gamma/2\pi$ (MHz)	$F_g$	$F_e$
$Q_1$	5.180	21.5	1.1	6.0	19.91	250	0.983	0.937
$Q_2$	5.930	17.2	1.5	14.3	20.92	238	0.990	0.920
$R$	5.581	12.9	234.5	-	-	-	-	-

TABLE S2: **Qubit and resonator characteristics.** The symbols  $Q_1$ ,  $Q_2$ , and  $R$  correspond to the test qubit, the ancilla qubit, and the resonator, respectively. The idle frequencies of  $Q_j$  ( $j = 1, 2$ ) and  $R$  are generally marked by  $\omega_{10}/2\pi$ , where single-qubit rotation pulses and measurements are applied. For the decoherence performance,  $T_1$  and  $T_2^*$  are the energy relaxation time and the Ramsey dephasing time (Gaussian decay), respectively, of  $Q_j$  and  $R$ , measured at the idle frequency. Additionally,  $T_2^{\text{SE}}$  is the dephasing time with spin echo (Gaussian decay). The coupling strength  $\lambda$  between  $Q_j$  and the bus resonator  $R$  is estimated via vacuum Rabi oscillations. The anharmonicity of the qubit is  $\gamma$ . The probability of detecting the qubit in  $|g\rangle$  ( $|e\rangle$ ) when it is prepared in  $|g\rangle$  ( $|e\rangle$ ) state is indicated by  $F_g$  ( $F_e$ ).

the superconducting qubits, e.g., see Ref. [S4], which reports similar control methods to our experiment.

The pulse sequences are shown in Fig. S2, including three steps: (I) SPT; (II) Wigner tomography; and (III) read-out of the photon-number distribution. Because the time span of several operations varies widely, real scales are not used.

### S3. CONTROL OF QUENCHING DYNAMICS

#### A. Time-dependence of the normalized coupling parameter $\xi$

During the quenching process, the normalized coupling parameter is changed as [S5]

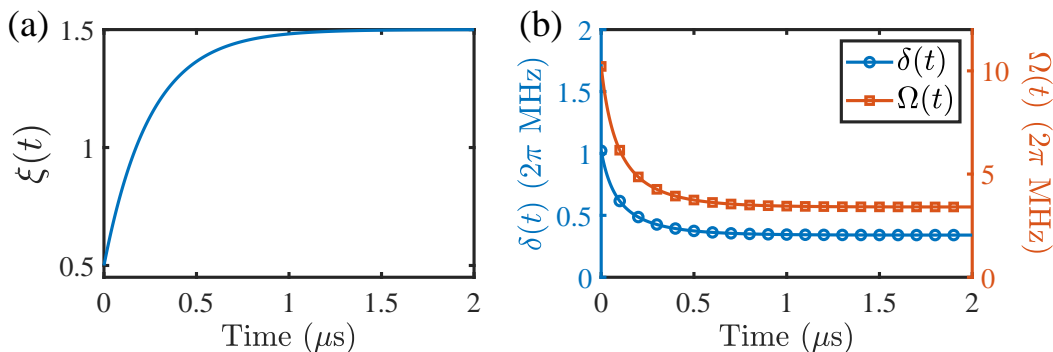


FIG. S3: (a) Normalized coupling parameter  $\xi(t)$  versus time. (b) Effective frequencies  $\delta(t)$  and  $\Omega(t)$  of the resonator and qubit versus time, showing on the left and right  $y$ -axes, respectively.

$$\xi(t) = (\xi_{\max} - \xi_0) \left[ 1 - \exp\left(-\frac{8t}{t_f}\right) \right] + \xi_0. \quad (\text{S20})$$

Here,  $\xi_{\max}$  ( $\xi_0$ ) is the maximum (initial) value of  $\xi(t)$  and  $t_f$  is the total evolution time. For Figs. 2 and 3 in the main text, we choose  $\xi_{\max} = 1.5$ ,  $\xi_0 = 0.5$ , and  $t_f = 2 \mu\text{s}$ . In addition, we choose  $\Omega = 10\delta$  at all times of the evolution to ensure the preset limitation  $\Omega \gg \delta$  of the SPT [S1]. The induced  $\xi(t)$ ,  $\Omega(t)$ , and  $\delta(t)$  are shown in Fig. S3.

The experiment starts by tuning the test qubit to the operating frequency  $\omega_0/2\pi = 5.18$  GHz, around which the two sine modulations are applied, with the fixed modulation frequencies  $\nu_1/2\pi = 200$  MHz and  $\nu_2/2\pi = 33.28$  MHz. The amplitude of the first modulation is set to  $\varepsilon_1/2\pi = 165.85$  MHz, while  $\varepsilon_2$  is taken as a control parameter. Near the operating frequency, the qubit is driven by a continuous microwave with Rabi frequency  $K/2\pi = 19.91$  MHz. For these settings, the dynamics of the test qubit and the resonator are governed by the Rabi Hamiltonian, with the qubit working in the frame rotating at the angular frequency  $B_0$  relative to the laboratory frame. The resulting effective qubit-resonator coupling strength is  $\eta/2\pi = 0.81$  MHz. During the Rabi dynamics, the ancilla qubit  $Q_2$  is far off-resonant with the test qubit  $Q_1$  and with the resonator, so that it remains in the ground state.

### B. Control of the effective qubit frequency $\Omega$

Because of the imperfect waveform of the periodically modulated excitation energy  $\hbar\omega_q(t)$ , we modify the first and second modulating pulses as  $\varepsilon_1 \cos(\nu_1 t + \phi_1^{\text{exp}})$  and  $\varepsilon_2 \cos(\nu_2 t + \phi_2^{\text{exp}})$ , respectively, to optimize the most appropriate dynamics of the Rabi Hamiltonian  $H_R$ . We iterate over different phases ( $\phi_1^{\text{exp}}, \phi_2^{\text{exp}}$ ) to carry out the experiments with setting  $\delta = 0$ , and finally obtain the one which best coincides with the corresponding simulated Rabi oscillation curves. The optimal results, specifically, for  $\Omega/2\pi = 3.6$  MHz, are shown in Fig. S4, where we can see that the fitting error (the Euclidean norm) becomes minimal when  $\phi_1^{\text{exp}} = 1.06\pi$  and  $\phi_2^{\text{exp}} = 1.00\pi$ . In this case, the concrete fitting situation is indicated in Fig. S5. The experimental data are intuitively close to the numerical fitting in Fig. S5, confirming the validity of such phase modification.

For convenience, we choose the same phase modifications (i.e.,  $\phi_1^{\text{exp}} = 1.06\pi$  and  $\phi_2^{\text{exp}} = 1.00\pi$ ) for different  $\Omega$  throughout the experiments. Note that we also slightly adjust the center frequencies and amplitudes of the two modulating pulses to improve the control.

### C. Control of the effective resonator frequency $\delta$

The control of the effective resonator frequency  $\delta(t)$  of the effective Rabi Hamiltonian in Eq. (S9) can be achieved by adjusting the Stark shift induced by the ancilla qubit  $Q_2$ . We can control this Stark shift by tuning the frequency of the ancilla qubit. When the detuning  $\Delta\omega$  between this ancilla qubit and the resonator is varied from  $\Delta\omega$  to  $\Delta\omega'$ , and remains much larger than their coupling strength  $\lambda'$ , the resulting resonator frequency shift becomes

$$\delta\omega_S = \frac{\lambda'^2}{\Delta\omega} - \frac{\lambda'^2}{\Delta\omega'}, \quad (\text{S21})$$

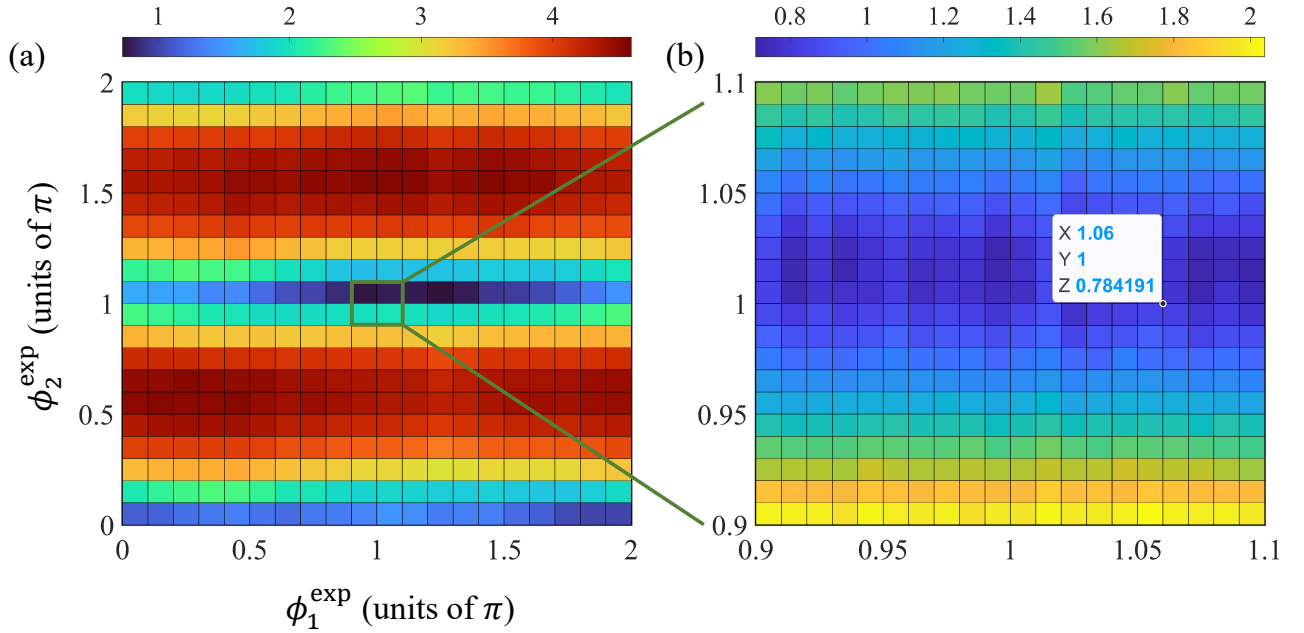


FIG. S4: (a) Fitting errors (Euclidean norm) versus phase modifications ( $\phi_1^{\text{exp}}$  and  $\phi_2^{\text{exp}}$ ) in the experiment. (b) Magnified view of (a) when  $\{\phi_1^{\text{exp}}, \phi_2^{\text{exp}}\} = [0.9, 1.1]\pi$ , where the optimal point used in the experiment has been marked.

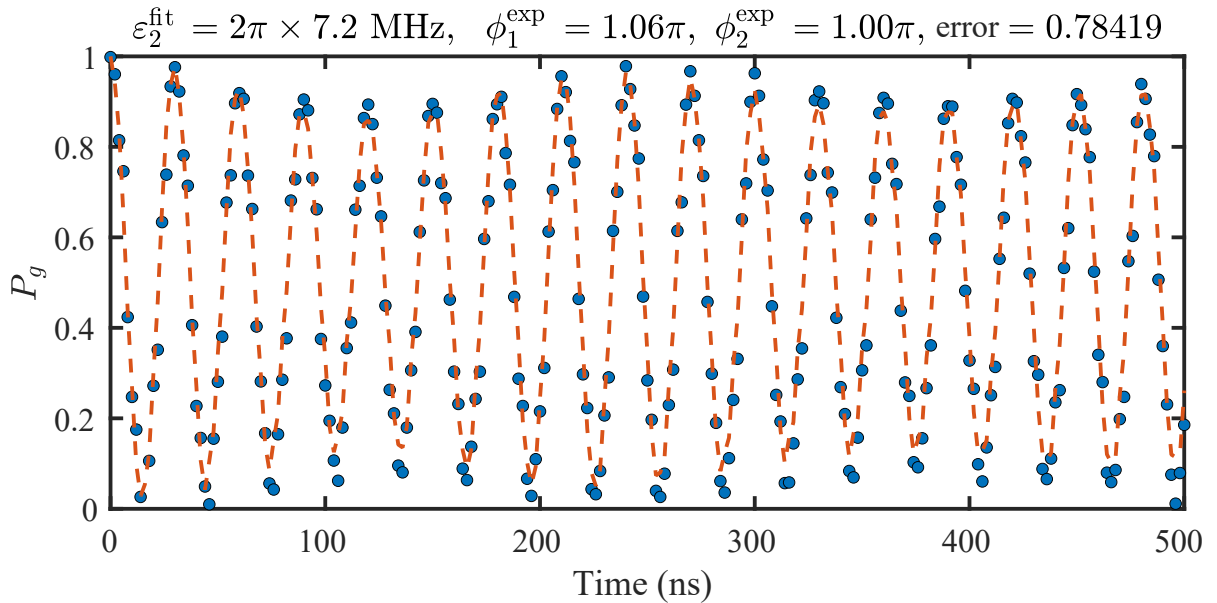


FIG. S5: Fitting for  $\phi_1^{\text{exp}} = 1.06\pi$  and  $\phi_2^{\text{exp}} = 1.00\pi$ . The populations  $P_g$  in the ground state of the test qubit  $Q_1$  versus time. The experiment data and the numerical results are marked by dots and a dashed curve, respectively.

where  $\lambda'/2\pi = 20.91$  MHz (different from  $\lambda$  in the main text). Equation (S21), in a different form, reads

$$\delta(t) - \delta(0) = \frac{\lambda'^2}{f(0) - \omega_p} - \frac{\lambda'^2}{f(t) - \omega_p}, \quad (\text{S22})$$

with  $f(t)$  being the transition frequency of the ancilla qubit. Based on Eq. (S22), we change  $f(t)$  from the idle frequency  $f_{\text{idle}}$ , viz.,  $f(0)/2\pi = f_{\text{idle}}/2\pi = 5.93$  GHz, yielding,



$$f(t) = \omega_p - \left[ \frac{\delta(t) - \delta(0)}{\lambda'^2} - \frac{1}{f_{\text{idle}} - \omega_p} \right]^{-1}. \quad (\text{S23})$$

To demonstrate the effectiveness of controlling  $\delta(t)$  experimentally, we apply square pulses with amplitudes  $f(t)$  ( $x$ -axis) to the Z-line of the ancilla qubit  $Q_2$ . Meanwhile, several square-envelope pulses with certain amplitudes and specific frequencies  $\omega_p + \delta(t)$  ( $y$ -axis) are applied to the XY-line of the test qubit  $Q_1$  to excite the resonator (by cross-talk interactions). Subsequently, we measure the populations of the ancilla qubit  $Q_2$  ( $z$ -axis) after a qubit-resonator-swap interaction (span time  $\pi/\lambda'$ ). This spectroscopy reflects the relationship between applying  $f(t)$  and the induced offset of the effective resonator frequency  $\delta(t)$ . After appropriately translating the  $y$ -axis and remapping values of  $f(t)$  to the corresponding time, we achieve the experimental control of  $\delta(t)$  as shown in Fig. S6, where the high-value populations (highlighted area) roughly depict the trend of the experimental  $\delta(t)$  and coincide well with its ideal values.

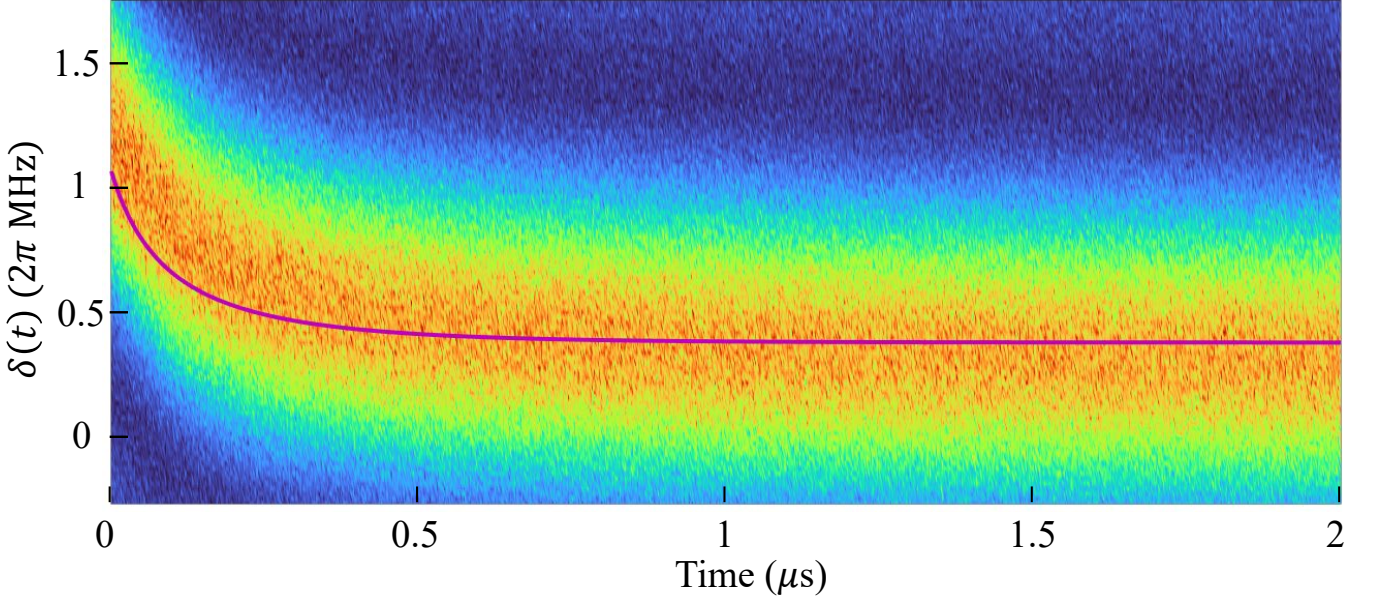


FIG. S6: Experimental frequency  $\delta(t)$  of the resonator versus time, induced by tuning the frequency of the ancilla qubit  $Q_2$  with a suitable translation added to the  $y$ -axis. The ideal  $\delta(t)$  is plotted with a solid purple-solid curve.

#### S4. EFFECTS OF OFF-RESONANT COUPLINGS AND DECOHERENCE

When considering high-energy levels of the Xmon qubit, the Hamiltonian becomes

$$H = H_0 + H_I, \quad (\text{S24})$$

$$H_0 = (\omega_0 + 2\nu_1)a^\dagger a + [\omega_0 + \varepsilon_1 \cos(\nu_1 t)]q^\dagger q - \frac{\gamma}{2}q^\dagger{}^2 q^2, \quad (\text{S25})$$

$$H_I = \delta a^\dagger a + (\lambda a^\dagger q + \text{h.c.}), \quad (\text{S26})$$

where  $q$  ( $q^\dagger$ ) denotes the annihilation (creation) operator for the Xmon qubit mode and  $\gamma$  is the anharmonicity of the qubit. For simplicity, we ignore the microwave driving  $K$  and the frequency modulation  $\varepsilon_2$ . Performing the transformation  $U_0$  and considering the lowest three levels of the Xmon qubit,  $\{|g\rangle, |e\rangle, |f\rangle\}$ , we obtain the system Hamiltonian in the rotating frame as

$$H'_I = \delta a^\dagger a + \left\{ \exp[-i\mu \sin(\nu_1 t)] \lambda \exp(2i\nu_1 t) a^\dagger [ |g\rangle \langle e| + \sqrt{2} \exp(i\gamma t) |e\rangle \langle f| ] + \text{h.c.} \right\}. \quad (\text{S27})$$

Using the Jacobi-Anger expansion, we obtain

$$H'_I = \delta a^\dagger a + \left( \sum_{n=-\infty}^{\infty} J_n(\mu) \lambda a^\dagger \left\{ \exp[-i(n-2)\nu_1 t] |g\rangle \langle e| + \sqrt{2} \exp[-i(n-2)\nu_1 t + i\gamma t] |e\rangle \langle f| \right\} + \text{h.c.} \right). \quad (\text{S28})$$

By assuming that  $\{|\lambda J_0(\mu)|, \delta\} \ll \nu_1$ ,  $H'_I$  reduces to the effective Hamiltonian

$$H_e = [J_2(\mu) \lambda a^\dagger] |g\rangle \langle e| + \text{h.c.} \\ + S_1(|g\rangle \langle g| - |e\rangle \langle e|) a^\dagger a - S_1 |e\rangle \langle e| + S_2 |e\rangle \langle e| a^\dagger a + \delta a^\dagger a, \quad (\text{S29})$$

where

$$S_1 \simeq \frac{[J_0(\mu)\lambda]^2}{2\nu_1} + \frac{[J_1(\mu)\lambda]^2}{\nu_1} + \frac{[J_{-1}(\mu)\lambda]^2}{3\nu_1}, \quad (\text{S30})$$

$$S_2 \simeq \frac{2[J_0(\mu)\lambda]^2}{2\nu_1 + \gamma} + \frac{2[J_1(\mu)\lambda]^2}{\nu_1 + \gamma} + \frac{2[J_{-1}(\mu)\lambda]^2}{3\nu_1 + \gamma}. \quad (\text{S31})$$

The term  $S_2 |e\rangle \langle e| a^\dagger a$  results from a dispersive coupling to the second-excited state  $|f\rangle$ .

Discarding the constant term, we can rewrite  $H_e$  as

$$H_e = H_{e,1} + H_{e,2}, \quad (\text{S32})$$

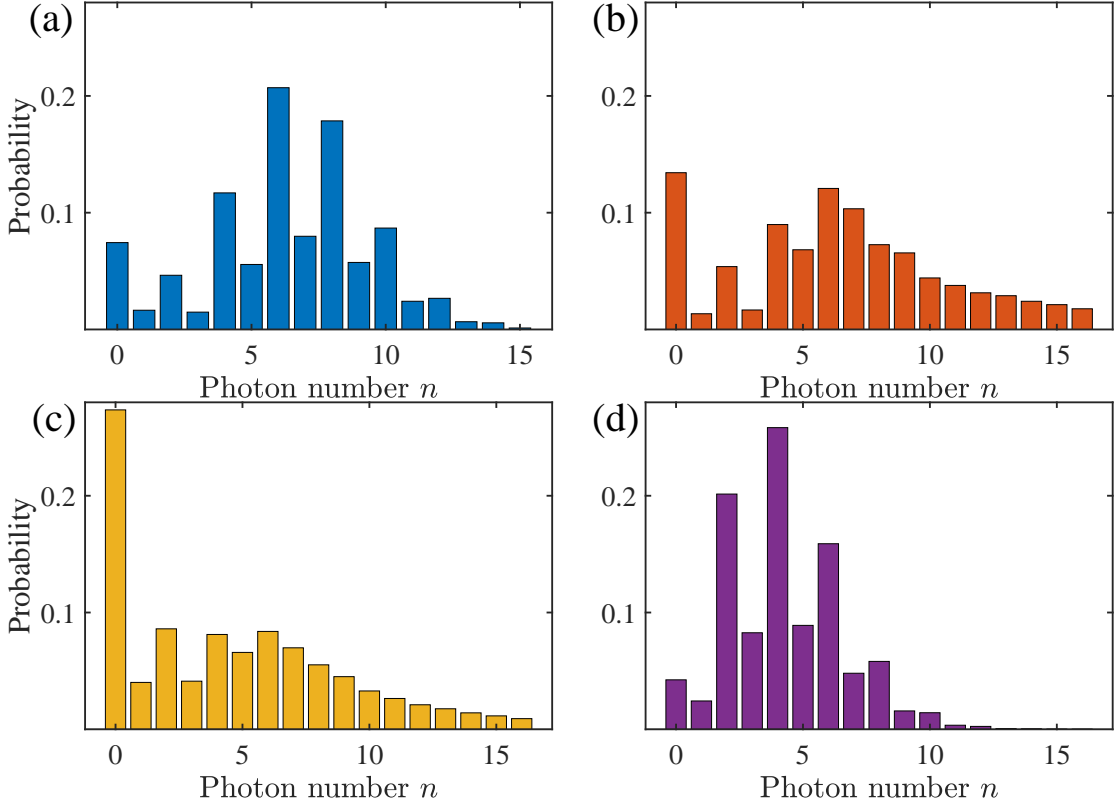


FIG. S7: Numerically simulated photon-number distributions of fields at  $t = 2 \mu\text{s}$ , which are calculated by the (a) effective Hamiltonian without decoherence, (b) full Hamiltonian without decoherence, and (c) full Hamiltonian with decoherence. (d) Ground state results of the effective Hamiltonian.

where

$$H_{e,1} = [J_2(\mu)\lambda a^\dagger] |g\rangle \langle e| + \text{h.c.}, \quad (\text{S33})$$

$$H_{e,2} = \left(S_1 - \frac{1}{2}S_2\right) (|g\rangle \langle g| - |e\rangle \langle e|) a^\dagger a + \frac{1}{2}S_1(|g\rangle \langle g| - |e\rangle \langle e|) + \left(\frac{1}{2}S_2 + \delta\right) a^\dagger a. \quad (\text{S34})$$

Therefore, the Stark shifts are significantly reduced when the effect of the second-excited state  $|f\rangle$  is considered. For the present device parameter setting, we obtain

$$S_1 - \frac{1}{2}S_2 \sim 2\pi \times 0.45 \text{ MHz}. \quad (\text{S35})$$

When the microwave drive is applied,  $H_{e,2}$  becomes

$$H'_{e,2} = \frac{(S_1 - \frac{1}{2}S_2)^2}{2K} \sigma_x (a^\dagger a)^2 + \frac{(\frac{1}{2}S_1)^2}{2K} \sigma_x + \left(\frac{1}{2}S_2 + \delta\right) a^\dagger a, \quad (\text{S36})$$

where

$$\frac{(S_1 - \frac{1}{2}S_2)^2}{2K} \simeq \frac{2\pi \times 0.45^2}{40} \text{ MHz} = 2\pi \times 0.0061 \text{ MHz}. \quad (\text{S37})$$

The first term of Eq. (S36) produces a qubit-state-dependent Kerr effect on the photonic field, dispersing the phase-space distributions of the coherent fields, which partly accounts for distortions of the observed Gaussian wavepackets. To quantitatively explore influences arising from imperfect Hamiltonian dynamics and decoherence, we perform numerical simulations on the photon-number distributions at  $t = 2 \mu\text{s}$ . Figures S7(a) and S7(b) present results based on the effective Rabi Hamiltonian and the full Hamiltonian, respectively; while Fig. S7(c) displays the result calculated by the master equation, including both the full Hamiltonian dynamics and decoherence. Figure S7(d) shows the photon number distributions associated with the ground state of the effective Rabi Hamiltonian. For the ground state of the ideal Rabi model with an infinite frequency ratio [S1], the vacuum component has a negligible population. Due to the experimental imperfections, the observed output state has a significant vacuum population of about 0.29. To quantify individual contributions to the vacuum population, we perform numerical simulations step by step, including more and more experimental imperfections. Thus obtained vacuum populations are respectively 0.07, 0.13, 0.27, and 0.04, as shown in Figs. S7(a)-(d). The results imply that the limitation of the effective qubit-resonator frequency ratio, non-adiabaticity, deviation from model Hamiltonian, and dissipation contribute vacuum populations of 0.04,  $0.07 - 0.04 = 0.03$ ,  $0.13 - 0.07 = 0.06$ , and  $0.27 - 0.13 = 0.14$ , respectively. We note the calculated vacuum population 0.27 in Fig. S7(c) is slightly smaller than the observed result 0.29 in Fig. 2 in the main text, mainly due to deviations of the system parameters used for the simulation from their real values. In the simulation, the dissipation times for the qubit and the resonator are the same as those listed in Table S2. These results clearly show that the population of the vacuum state is mainly caused by decoherence.

Note that there are also two corrections in the numerical simulation for the master equation: (i) applying  $\Omega(t)' = 1.56 \Omega(t)$  [ $\Omega(t)$  shown in Fig. S3]; (2) utilizing the fitting  $\delta'(t)$  deduced by experimental measurements in Fig. S6, shown in Fig. S8.

The simulated average photon number has shown in Fig. 2 in the main text. Additionally, based on such numerical simulation, we plot the corresponding Wigner functions in Fig. S9. We also plot the population of the third level  $|f\rangle$  in Fig. S10, when the  $|f\rangle$  is included in the numerical simulation. The results show that the average population of the third level is about 0.11 during the quenching dynamics.

## S5. CHARACTERIZATION OF THE QUBIT-RESONATOR STATE

### A. Photon-number distribution

All the measured average photon numbers and the Wigner function values in the main text are deduced from the photon-number distribution. In the experiment, after carrying out the part of the SPT (or after Wigner tomography),

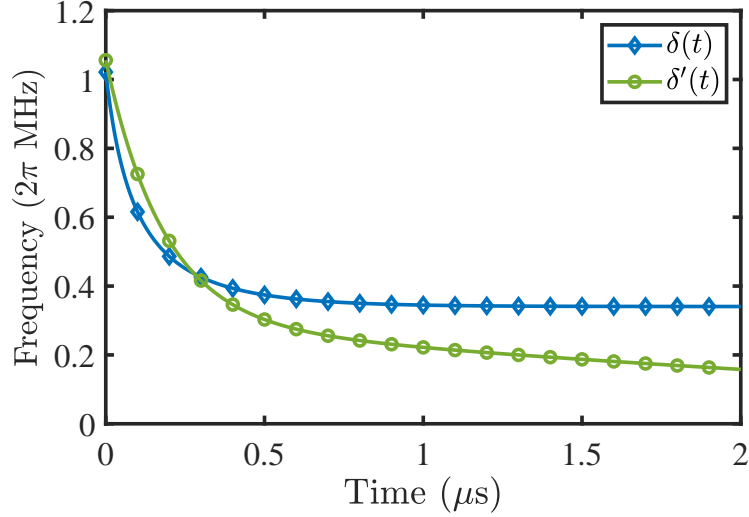


FIG. S8: Effective resonator frequency versus time. The green line with circular markers represents the fitting effective resonator frequency  $\delta'(t)$  deduced by experimental measurements in Fig. S6. The blue line with diamond markers indicates the ideal effective resonator frequency.

the microwave drive  $K$  and the frequency modulations  $\omega_q$  are switched off. Meanwhile, the ancilla qubit  $Q_2$  is tuned on resonance with the resonator (frequency 5.581 GHz) from the idle frequency 5.93 GHz. Furthermore, the ancilla qubit  $Q_2$  undergoes photon-number-dependent Rabi oscillations. The populations  $P_e^a(\tau)$ , of the excited state of the ancilla qubit  $Q_2$  for a given interaction time  $\tau$ , are measured by biasing the ancilla back to its idle frequency, where its state is read out (intuitively see Fig. S2). The recorded time-resolved quantum Rabi oscillation signals can be fitted as

$$P_e^a(\tau) = \frac{1}{2} \left[ 1 - P_g^a(0) \sum_{n=0}^{n_{\max}} P_n e^{-\kappa_n \tau} \cos(2\sqrt{n}\lambda'\tau) \right], \quad (\text{S38})$$

where  $P_n$  denotes the photon-number distribution probability,  $P_g^a(0)$  indicates the probability for the ancilla qubit  $Q_2$  to start in the ground state,  $n_{\max}$  is the cutoff of the photon number, and  $\kappa_n = n^l/T_{1,p}$  ( $l = 0.7$ ) [S6–S10] is the empirical decay rate of the Rabi oscillations associated with the  $n$ -photon state. It is worth mentioning that, when there are a lot of photons in the resonator, especially  $\langle a^\dagger a \rangle > 10$ , the detuning  $\Delta\omega/2\pi = (5.93 - 5.581)$  GHz = 0.329 GHz is not large enough to avoid interactions between the ancilla qubit  $Q_2$  and the resonator. This induces a minor excitation of the ancilla qubit  $Q_2$ , depending on the excitation of the resonator. Thus, referring to [S6], we ignore the small excitation of  $|e\rangle$  and rescale the factor  $1/2$  in the photon-number-dependent Rabi oscillations equation [S10], to  $P_g(0)/2$  [see Eq. (S38)]. Based on the measurements and fitting operations described above, we can give the fitting situation and corresponding photon-number distribution in Fig. S11.

### B. Diagonal Wigner matrix elements

As described in the main text, the Wigner function is given by

$$\mathcal{W}_{k,k'}(\beta) = \frac{2}{\pi} \sum_{n=0}^{\infty} (-1)^n \mathcal{P}_n^{k,k'}(\beta), \quad (\text{S39})$$

where

$$\mathcal{P}_n^{k,k'}(\beta) = \langle n | D(-\beta) \rho_{k,k'} D(\beta) | n \rangle. \quad (k, k' = e, g)$$



To measure the Wigner diagonal elements, a displacement operation,  $D(\beta) = \exp(\beta a^\dagger - \beta^* a)$ , is applied to the resonator, following which the ancilla qubit  $Q_2$  is resonantly coupled to the resonator for a given time  $\tau$ . Then, the ancilla qubit  $Q_2$  is biased to the idle frequency for the read-out of states.

The photon-number distributions  $\mathcal{P}_n^{g,g}(\beta)$  and  $\mathcal{P}_n^{e,e}(\beta)$  of the displaced light field are associated with the test qubit states  $|g\rangle$  and  $|e\rangle$ . Such distributions can be extracted from the excited-state populations  $[P_{n,e}^g(\beta, \tau)$  and  $P_{n,e}^e(\beta, \tau)]$  of the ancilla qubit, conditional on the detection of the test qubit in states  $|g\rangle$  and  $|e\rangle$ . Thus, the normalized Wigner function (for diagonal elements in the qubit basis) is given by

$$W_{k,k}(\beta) = \mathcal{W}_{k,k}(\beta)/P_k, \quad (\text{S40})$$

with  $P_k$  being the  $|k\rangle$ -state population of the test qubit. To completely show the distribution of the generated cat states in phase space, we calibrate  $\{\text{Re}(\beta), \text{Im}(\beta)\} \in [-3, 3]$ , implying that the displacement distance of  $D(-\beta)$ , i.e.,  $|\beta|$ , can be up to  $3\sqrt{2}$ . This leads to the fact that the displaced light fields in some cases process an average photon number  $\langle a^\dagger a \rangle \gtrsim 18$ .

However, as claimed in Sec. S5 A, the read-out of the photon-number distribution becomes imprecise with photons growing. We therefore ignore the areas with large numbers of photons and utilize the remaining areas to deduce the normalized density matrix  $\rho_{k,k}/P_k$  of light fields. This treatment is intuitively shown in Fig. S12. The calculation from the Wigner function  $W_{k,k}(\beta)$  to the density matrix  $\rho_{k,k}/P_k$  is completed using convex optimization, supported by

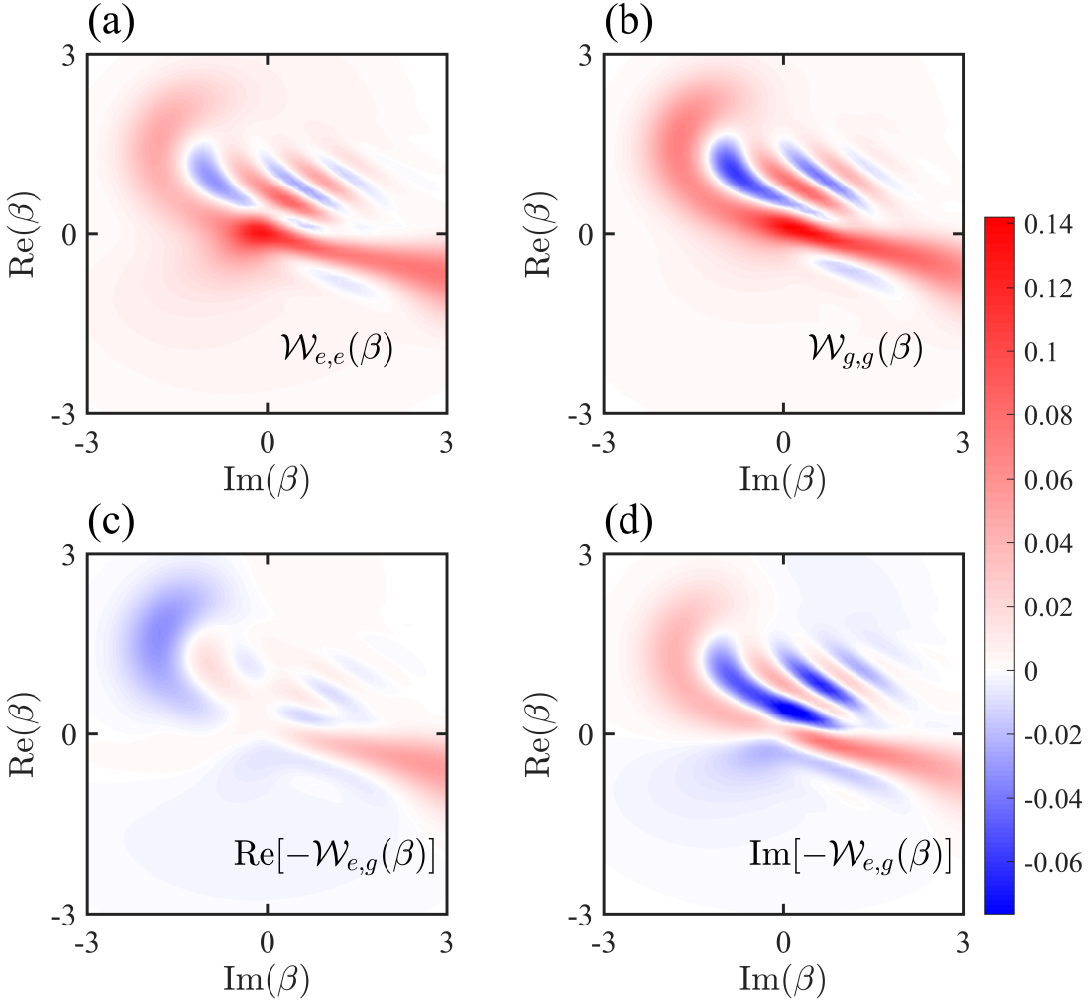


FIG. S9: Numerically simulated Wigner matrix tomography. (a–d) Corresponds to Fig. 3 (a–d) in the main text, respectively. Note that suitable rotations of Wigner tomography have been applied and all the data are measured at  $t = 2 \mu\text{s}$  based on the parameter corrections in Sec. S4.

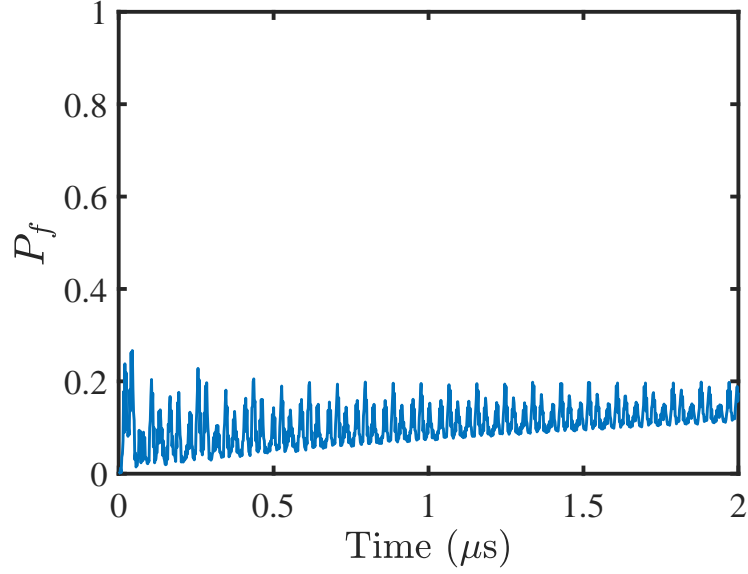


FIG. S10: Numerically simulated population of the third level  $|f\rangle$ .

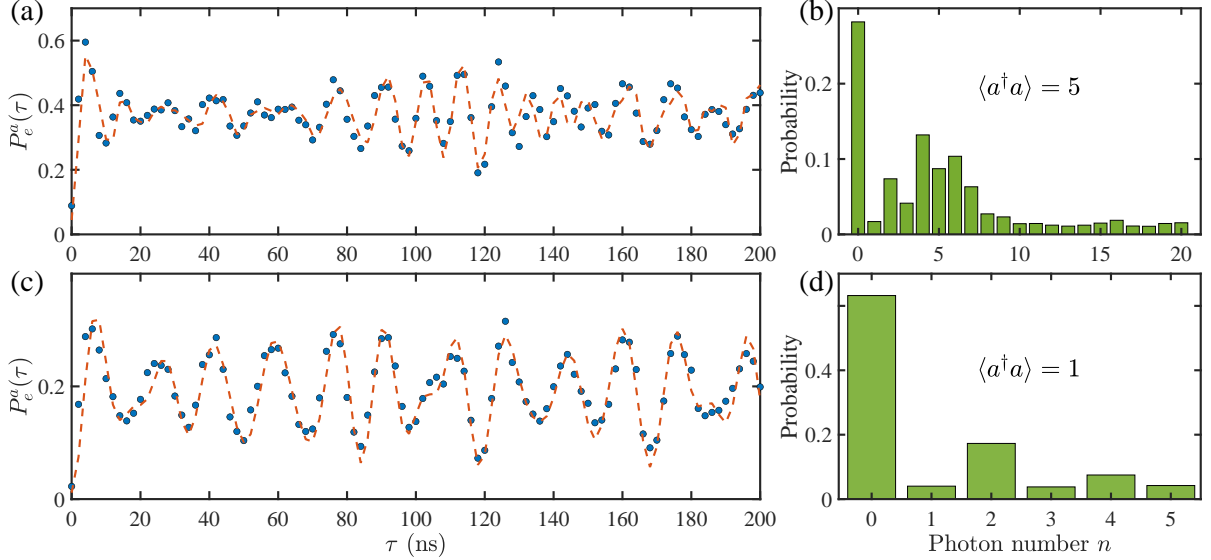


FIG. S11: Experimental (dots) and theoretical (dashed curves) time-resolved quantum Rabi oscillations and corresponding photon-number distributions for (a, b)  $\langle a^\dagger a \rangle = 5$  and (c, d)  $\langle a^\dagger a \rangle = 1$ .

the CVX toolbox based on MATLAB [S11]. The solved density matrix  $\rho_{k,k}/P_k$  is Hermitian and positive semidefinite as well as satisfying  $\text{Tr}(\rho_{k,k}/P_k) = 1$ . Furthermore, we use this solved  $\rho_{k,k}/P_k$  to plot  $\mathcal{W}_{k,k}(\beta)$ , shown in Figs. 3(a) and 3(b) in the main text, which has the same distribution in phase space as Figs. S12(a) and S12(b) here. As for Figs. 3(c) and 3(d) in the main text, we additionally perform Wigner tomography (detailed in the next section) and take the same treatment as that for Figs. S12(a) and S12(b). The time to measure the Wigner function is  $t = 1.946 \mu\text{s}$  because the error of the qubit projection is relatively small at this time.

### C. Off-diagonal Wigner matrix elements

To fully characterize the nonclassical light-matter correlations, it is necessary to reconstruct the off-diagonal elements, measurements of which require Wigner tomography in the rotated basis  $\{|\pm_x\rangle = (|e\rangle \pm |g\rangle)/\sqrt{2}\}$  and

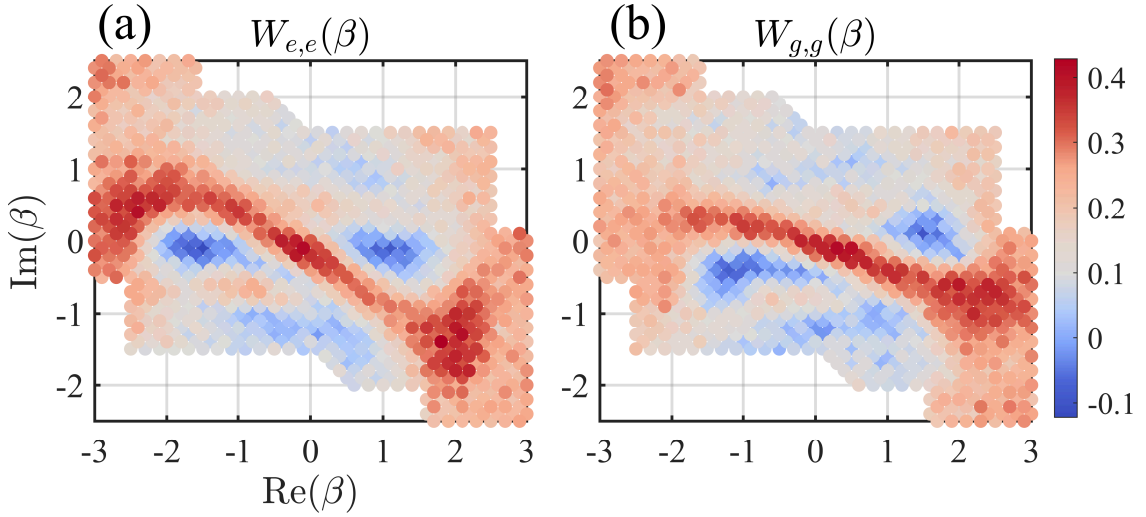


FIG. S12: Experimental data of the Wigner functions (a)  $W_{e,e}(\beta)$  and (b)  $W_{g,g}(\beta)$ , without displaying the points corresponding to large numbers of photons ( $\langle a^\dagger a \rangle > 10$ ).

$\{|\pm_y\rangle\} = \{|e\rangle \pm i|g\rangle/\sqrt{2}\}$ , respectively. The Wigner diagonal elements in these bases are related to both diagonal and off-diagonal elements in the basis  $\{|e\rangle, |g\rangle\}$ :

$$\mathcal{W}_{\pm x, \pm x}(\beta) = \frac{1}{2}[\mathcal{W}_{e,e}(\beta) + \mathcal{W}_{g,g}(\beta)] \pm \text{Re}[\mathcal{W}_{e,g}(\beta)], \quad (\text{S41})$$

$$\mathcal{W}_{\pm y, \pm y}(\beta) = \frac{1}{2}[\mathcal{W}_{e,e}(\beta) + \mathcal{W}_{g,g}(\beta)] \mp \text{Im}[\mathcal{W}_{e,g}(\beta)]. \quad (\text{S42})$$

To measure the Wigner matrix element  $\mathcal{W}_{+x,+x}(\beta)$ , a rotation  $R_y(\pi/2)$  is performed on the test qubit  $Q_1$  before its state read-out, transforming the  $x$ -axis basis states  $|+x\rangle$  and  $|-x\rangle$  to the  $z$ -axis basis states  $|e\rangle$  and  $|g\rangle$ , respectively, which can be directly measured by the read-out resonator. After this rotation and the resonator displacement  $D(-\beta)$ , the measured photon-number distribution  $\mathcal{P}_n^{e,e}(\beta)$ , conditional on the detection of the test qubit state  $|e\rangle$ , yields the conditional Wigner function  $W_{+x,+x}(\beta)$ . Similarly, performing the resonator displacement  $D(-\beta)$  after a qubit rotation  $R_x(\pi/2)$ , we can reconstruct the conditional Wigner function  $W_{+y,+y}$  based on the measured photon-number distribution  $\mathcal{P}_n^{e,e}(\beta)$ . The elements  $\mathcal{W}_{\pm J, \pm J}(\beta)$  ( $J = x, y$ ) are related to the normalized Wigner function  $W_{\pm J, \pm J}(\beta)$  by

$$\mathcal{W}_{\pm J, \pm J}(\beta) = P_{\pm J}^{e(g)} W_{\pm J, \pm J}(\beta), \quad (\text{S43})$$

where  $P_J^{e(g)}$  denotes the  $|e\rangle|g\rangle$ -state population of the test qubit  $Q_1$  after the corresponding frame transformation. Moreover, the real and imaginary parts of the off-diagonal element  $\mathcal{W}_{e,g}(\beta)$ , can be calculated by

$$\begin{aligned} \text{Re}[\mathcal{W}_{e,g}(\beta)] &= \frac{1}{2}[\mathcal{W}_{+x,+x}(\beta) - \mathcal{W}_{-x,-x}(\beta)], \\ \text{Im}[\mathcal{W}_{e,g}(\beta)] &= \frac{1}{2}[\mathcal{W}_{-y,-y}(\beta) - \mathcal{W}_{+y,+y}(\beta)]. \end{aligned} \quad (\text{S44})$$

Note that  $\mathcal{W}_{\pm x, \pm x}$  and  $\mathcal{W}_{\pm y, \pm y}$  can be described the same as  $\mathcal{W}_{k,k}$  in Sec. S5 B. The images of  $\text{Re}[-\mathcal{W}_{e,g}(\beta)]$  and  $\text{Im}[\mathcal{W}_{e,g}(\beta)]$  are shown in Figs. 3(c) and 3(d) in the main text, respectively.

## S6. MEASURE OF THE QUBIT-RESONATOR ENTANGLEMENT

The partial transpose of the density matrix is

$$\rho^{\Gamma Q} = \sum_{k=e,g} \sum_{k'=e,g} \rho_{k',k} \otimes |k\rangle\langle k'|, \quad (\text{S45})$$

whose eigenvalues are defined as  $E_i$ . The negativity [S12] is the absolute sum of the negative eigenvalues, viz.,  $\mathcal{N}(\rho) = |\sum_{E_i < 0} E_i| = 0.2483$ . For comparison, the upper bound of the negativity, is  $\mathcal{N}(|\psi_{\text{sp}}\rangle\langle\psi_{\text{sp}}|) = 0.4483$ . The difference between the experimental negativity and the ideal one is mainly due to the influence of decoherence, demonstrated by the loss of the purity of the density matrix from 1 to 0.4646.

## S7. CHARACTERIZATION OF THE SUPER-CAT STATE

Due to the non-adiabatic effects and the presence of decoherence, the emergent cat state during the SPT contains three superimposed components: one corresponding to the empty field mode, while the other two corresponding to the emergent coherent fields with opposite phases, as illustrated in Fig. S13. The size of this super-cat state is given by

$$\mathcal{S} = \frac{\sum_{s \neq l} d_{sl}^2 \sqrt{P_s P_l}}{\sum_{s \neq l} \sqrt{P_s P_l}}, \quad (\text{S46})$$

with  $\{s, l\} = \{|0\rangle, |\alpha\rangle, |-\alpha\rangle\}$  and  $d_{sl}^2$  indicating the square of the phase-space distance between  $s$  and  $l$ . Here  $P_{|0\rangle}$ ,  $P_{|\alpha\rangle}$ , and  $P_{|-\alpha\rangle}$  are the populations in  $|0\rangle$ ,  $|\alpha\rangle$ , and  $|-\alpha\rangle$  of  $\rho_{e,e}/\text{Tr}(\rho_{e,e})$  [or  $\rho_{g,g}/\text{Tr}(\rho_{g,g})$ ], respectively. For the three-components cat-like state, mixing  $|0\rangle$ ,  $|\alpha\rangle$ , and  $|-\alpha\rangle$ , Eq. (S46) becomes

$$\mathcal{S} = \frac{\sqrt{P_{|0\rangle} P_{|\alpha\rangle}} |\alpha|^2 + \sqrt{P_{|0\rangle} P_{|-\alpha\rangle}} |\alpha|^2 + \sqrt{P_{|\alpha\rangle} P_{|-\alpha\rangle}} |2\alpha|^2}{\sqrt{P_{|0\rangle} P_{|\alpha\rangle}} + \sqrt{P_{|0\rangle} P_{|-\alpha\rangle}} + \sqrt{P_{|\alpha\rangle} P_{|-\alpha\rangle}}}, \quad (\text{S47})$$

specifically,  $\mathcal{S}_{e,e} = 14.03$  and  $\mathcal{S}_{g,g} = 13.27$  for  $\rho_{e,e}/\text{Tr}(\rho_{e,e})$  and  $\rho_{g,g}/\text{Tr}(\rho_{g,g})$ , respectively.

The NP-SP quantum coherences associated with the qubit states  $|e\rangle$  and  $|g\rangle$  are

$$\mathcal{C}_{e,e} = \sum_{n=1}^{\infty} |\langle 0|\rho_{e,e}|n\rangle|/\text{Tr}(\rho_{e,e}) = 1.018, \quad \text{and} \quad \mathcal{C}_{g,g} = \sum_{n=1}^{\infty} |\langle 0|\rho_{g,g}|n\rangle|/\text{Tr}(\rho_{g,g}) = 1.020, \quad (\text{S48})$$

respectively. The quantum coherence averaged over these two super-cat states is 1.019.

Negative values of the Wigner functions clearly distinguish cat states, which are macroscopically-distinct coherent superpositions of classical-like states, from their mixtures. These negative values (as shown by the blue regions in Figs. S9 and S12, as well as Fig. 3 in the main text), which are clearly seen between the main peaks (as shown on the left- and right-hand sides of the figures), occur as a result of interference in the phase space [S13]. In the digital quantum simulation of the deep-strong coupling dynamics reported in Ref. [S14], a similar nonclassical state was generated by repetitive application of digital  $\pi$  pulses interleaved with short Jaynes-Cummings (JC) interaction without the counter-rotating-wave terms, which allows emulation of the long-time Rabi dynamics, but does not lead to the simultaneous realization of the JC and anti-JC interactions necessary for observing the associated SPT.

## S8. NUMERICAL SIMULATION OF THE DICKE-MODEL SPT

Pushing one step further, we theoretically extend our method to the Tavis-Cummings (TC) model involving multiple qubits coupled to a resonator [S15, S16]. By longitudinally modulating and transversely driving each qubit, the TC model can be effectively transformed to the Dicke model with similar parameters. The results show that the qubits-resonator system can be evolved from the NP to the SP featuring a highly entangled cat state, formed by two photonic coherent states with opposite phases that are nonclassically correlated with distinct multiqubit coherent states also with opposite phases.

The Dicke model, composed of  $N$  qubits coupled to a quantum photonic field mode, is described by the Hamiltonian

$$H_D = \delta a^\dagger a + \sum_{j=1}^N \left[ \frac{\Omega}{2} (|e_j\rangle\langle e_j| - |g_j\rangle\langle g_j|) \right]$$

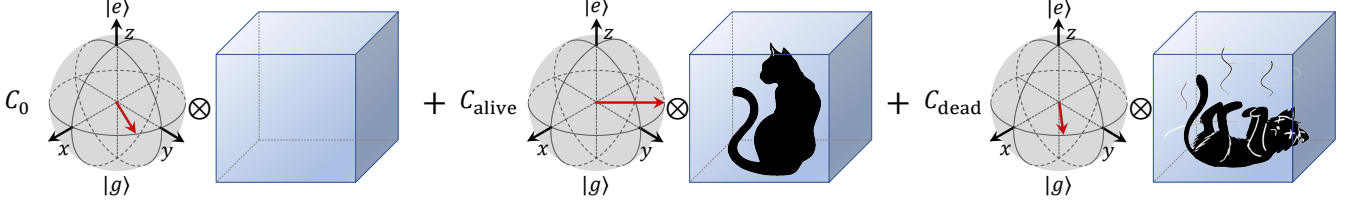


FIG. S13: Pictorial illustration of the three-component cat state. The resonator is in a superposition of being empty (without any cat) and containing a coherent field, which is formed by two superimposed components with complex amplitude  $\alpha$  (alive cat) and  $-\alpha$  (dead cat). These field components are correlated with different Bloch vectors (red-arrow lines) of the qubit.

$$+ \frac{\eta}{\sqrt{N}} (|e_j\rangle \langle g_j| + |g_j\rangle \langle e_j|) (a^\dagger + a), \quad (\text{S49})$$

where  $\eta$  denotes the collective qubit-field coupling strength, and  $|g_j\rangle$  and  $|e_j\rangle$  denoting the ground and excited states of the  $j$ th qubit, respectively. In the thermal limit  $N \rightarrow \infty$ , the system undergoes a SPT at the critical point  $\xi = 2\eta/\sqrt{\Omega\delta} = 1$  [S17]. When  $\xi$  is sufficiently large the system has two degenerate ground states, given by [S18]

$$|\psi_{sp}^\pm\rangle \simeq \frac{1}{\sqrt{2}} [|\alpha'\rangle \prod_{j=1}^N |+_j\rangle \pm |-\alpha'\rangle \prod_{j=1}^N |-_j\rangle], \quad (\text{S50})$$

where  $|\pm_j\rangle = (|g_j\rangle \pm |e_j\rangle)/\sqrt{2}$ , and  $|\pm\alpha'\rangle$  represent the coherent states of the photonic field, with  $\alpha' = \frac{\sqrt{N}\lambda}{\delta} \sqrt{1 - \xi^{-2}}$ . For the even-parity ground state  $|\psi_{sp}^+\rangle$ , the field parts associated with the even and odd collective excitation numbers of the qubits are even and odd cat states,  $|C_\pm\rangle = (|\alpha'\rangle \pm |-\alpha'\rangle)/\sqrt{2}$ , respectively.

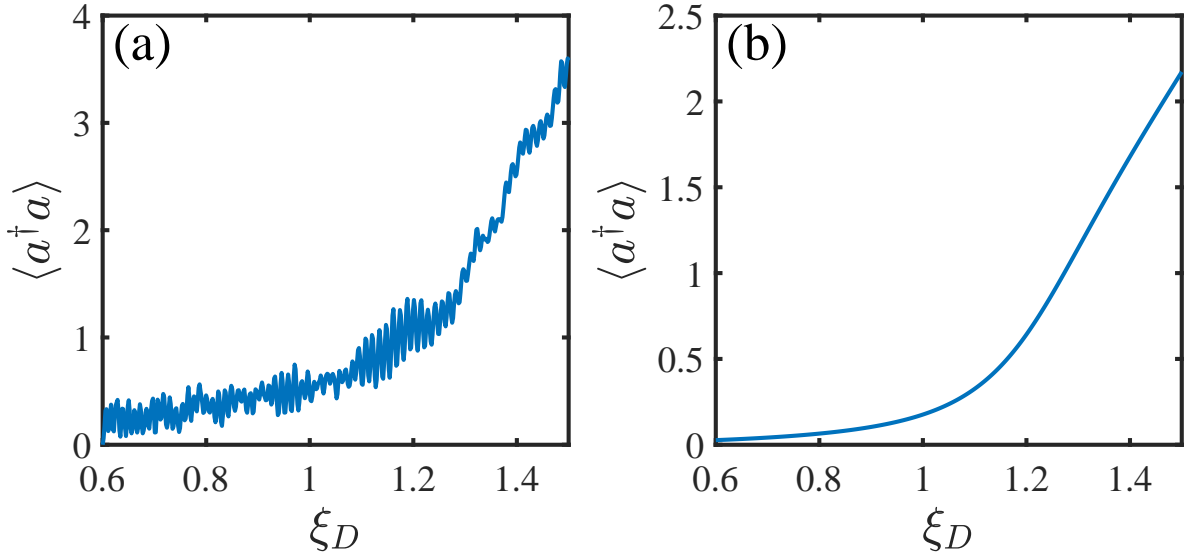


FIG. S14: Numerically simulated average photon number. (a) Result governed by full Hamiltonian. (b) Result deduced by even ground state of the Dicke-model Hamiltonian.

When the coupling strength  $\lambda$  between each qubit and the resonator is much smaller than the qubits' frequency  $\omega_0$  and the field frequency  $\omega_p$ , the counter-rotating-wave terms for realizing the Dicke SPT can be effectively realized by applying a resonant transverse driving with the amplitude  $K$ , and two longitudinal modulations with frequencies  $\nu_1$  and  $\nu_2$  and amplitudes  $\varepsilon_1$  and  $\varepsilon_2$ , to each of the qubit. Under the conditions  $\lambda, K, \delta = \omega_p - \omega_0 - 2\nu_1 \ll \nu_1$  and

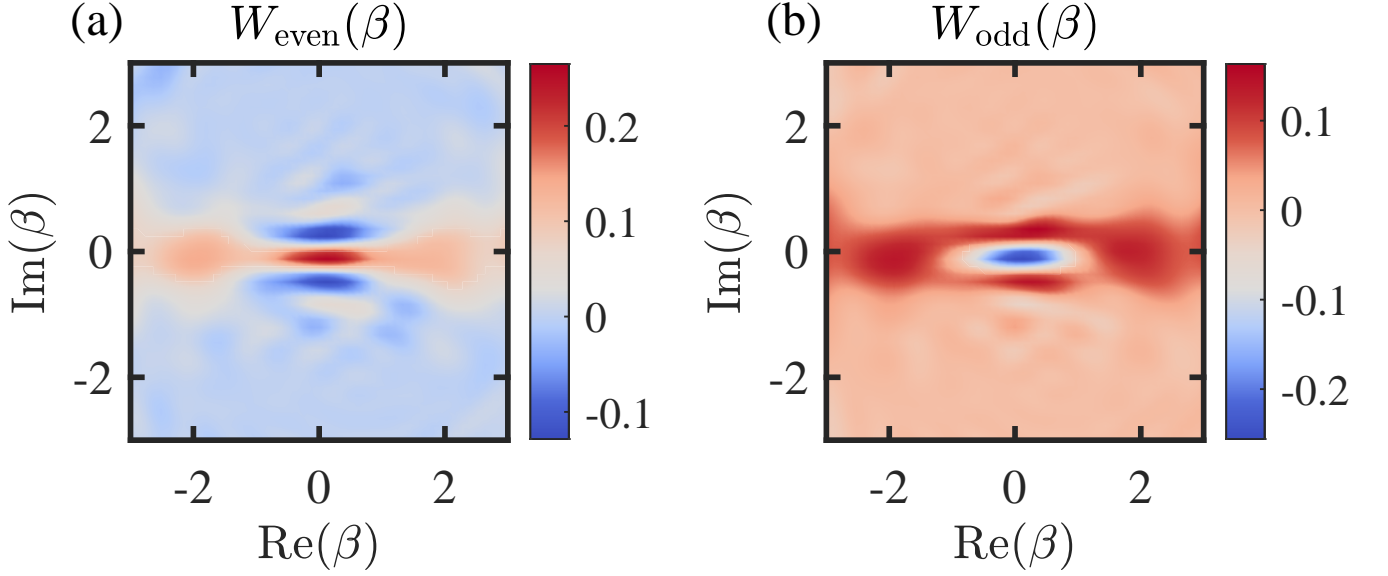


FIG. S15: Numerical Wigner tomography for final state after the Dicke-model SPT, governed by the full Hamiltonian. (a) Wigner functions associated with the collective even-parities of the qubits. (b) Wigner functions associated with the collective odd-parities of the qubits.

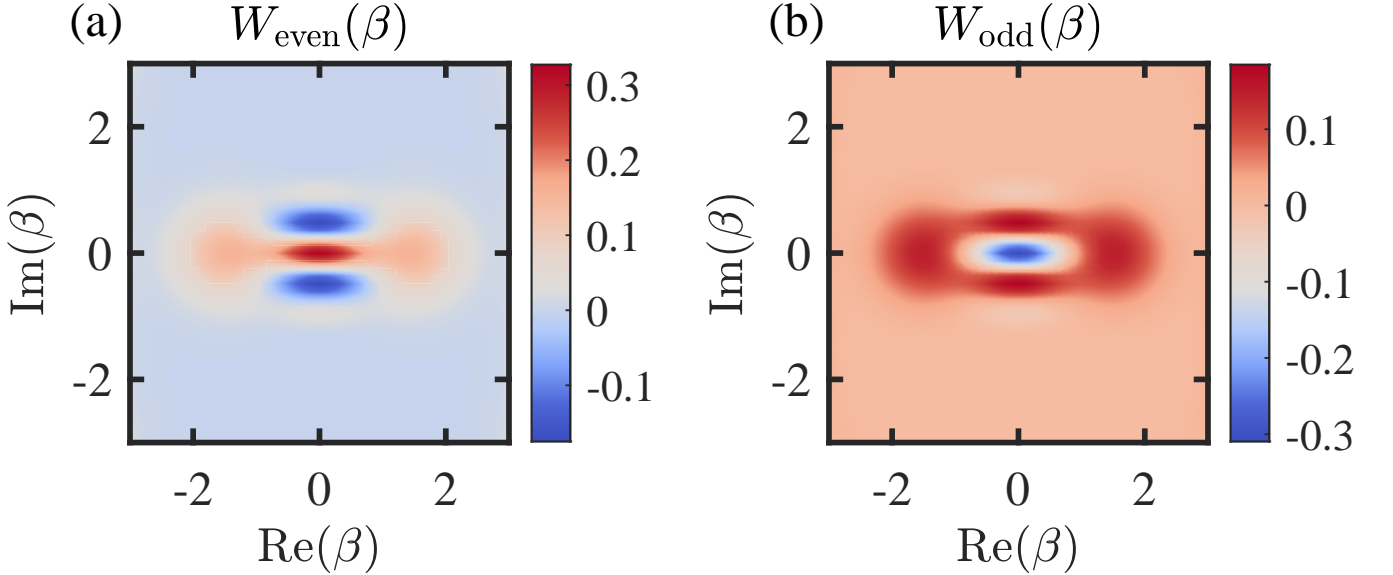


FIG. S16: Numerical Wigner tomography for final state after the Dicke-model SPT, deduced by the ground state of the Dicke-model Hamiltonian. (a) Wigner functions associated with the collective even-parities of the qubits. (b) Wigner functions associated with the collective odd-parities of the qubits.

$\nu_2 = 2KJ_0(\mu)$  with  $\mu = \varepsilon_1/\nu_1$ , the system dynamics in the interaction picture can be effectively described by the Dicke Hamiltonian with  $\eta = \sqrt{N}\lambda J_2(\mu)/2$  and  $\Omega = \varepsilon_2/2$ .

To confirm the validity of the approximations for deriving the effective Hamiltonian, we perform numerical simulations for the 10-qubit Dicke model, in the symmetric Dicke subspace, without considering decoherence. We here set  $\omega_p/(2\pi) = 5.581$  GHz,  $\lambda/(2\pi) = 19.91$  MHz,  $K/(2\pi) = 19.91$  MHz,  $\varepsilon_1/(2\pi) = 207.31$  MHz,  $\nu_1/(2\pi) = 250$  MHz, and  $\nu_2/(2\pi) = 33.28$  MHz. With this setting,  $\xi$  can be controlled by  $\omega_0$  and  $\varepsilon_2$ . With this setting,  $\xi$  can be controlled by  $\omega_0$  and  $\varepsilon_2$ . The average photon number, simulated for the quenching process where  $\delta$  and  $\varepsilon_2$  are varied as  $\delta = \varepsilon_2 = 2\eta/\xi(t)$ , with  $\xi(t) = 0.6 + 0.9t/t_f$  ( $t_f$  the total quench time), is shown in Fig. S14(a), which well agrees with

the result obtained from the even ground state of the ideal Hamiltonian (Fig. S14(b)). The quenching process starts with the state  $|0\rangle \prod_{j=1}^N |g_j\rangle$ . The Wigner functions of the field, associated with the collective even- and odd-parities of the qubits after a quenching time  $t = 2 \mu\text{s}$ , are respectively displayed in Figs. S15(a) and S15(b). These field states are in well agreement with those based on the ideal ground states with the same parameter  $\xi$ , displayed in Figs. S16(a) and S16(b), respectively. These results imply that the presently demonstrated techniques can be used to realize the Dicke model and the associated SPT.

- 
- [S1] M.-J. Hwang, R. Puebla, M. B. Plenio, “Quantum phase transition and universal dynamics in the Rabi model,” *Phys. Rev. Lett.* **115**, 180404 (2015).
- [S2] C. Song *et al.*, “Continuous-variable geometric phase and its manipulation for quantum computation in a superconducting circuit,” *Nat. Commun.* **8**, 1061 (2017).
- [S3] W. Ning *et al.*, “Deterministic entanglement swapping in a superconducting circuit,” *Phys. Rev. Lett.* **123**, 060502 (2019).
- [S4] C. Song *et al.*, “10-qubit entanglement and parallel logic operations with a superconducting circuit,” *Phys. Rev. Lett.* **119**, 180511 (2017).
- [S5] Q.-X. Mei *et al.*, “Experimental realization of the Rabi-Hubbard model with trapped ions,” *Phys. Rev. Lett.* **128**, 160504 (2022).
- [S6] M. Hofheinz *et al.*, “Synthesizing arbitrary quantum states in a superconducting resonator,” *Nature* **459**, 546–549 (2009).
- [S7] D. M. Meekhof, *et al.*, “Generation of nonclassical motional states of a trapped atom,” *Phys. Rev. Lett.* **76**, 1796–1799 (1996).
- [S8] D. Leibfried, *et al.*, “Quantum dynamics of single trapped ions,” *Rev. Mod. Phys.* **75**, 281–324 (2003).
- [S9] D. Lv *et al.*, “Quantum simulation of the quantum Rabi model in a trapped ion,” *Phys. Rev. X* **8**, 021027 (2018).
- [S10] M.-L. Cai *et al.*, “Observation of a quantum phase transition in the quantum Rabi model with a single trapped ion,” *Nat. Commun.* **12**, 1126 (2021).
- [S11] M. Grant, S. Boyd, CVX: Matlab software for disciplined convex programming, version 2.0 beta. <http://cvxr.com/cvx>, September (2013).
- [S12] G. Vidal, R. F. Werner, “Computable measure of entanglement,” *Phys. Rev. A* **65**, 032314 (2002).
- [S13] W. P. Schleich, “Quantum Optics in Phase Space,” (Wiley-VCH, Berlin, 2001).
- [S14] N. K. Langford *et al.*, “Experimentally simulating the dynamics of quantum light and matter at deep-strong coupling,” *Nat. Commun.* **8**, 1715 (2017).
- [S15] M. Tavis, F. W. Cummings, “Exact solution for an  $N$ -molecule-radiation-field Hamiltonian,” *Phys. Rev.* **170**, 379 (1968).
- [S16] C. Song *et al.*, “Generation of multicomponent atomic Schrödinger cat states of up to 20 qubits,” *Science* **365**, 574 (2019).
- [S17] Clive Emary, Tobias Brandes, “Quantum chaos triggered by precursors of a quantum phase transition: The Dicke model,” *Phys. Rev. Lett.* **90**, 044101 (2003).
- [S18] Pierre Nataf, Cristiano Ciuti, “Protected quantum computation with multiple resonators in ultrastrong coupling circuit QED,” *Phys. Rev. Lett.* **107**, 190402 (2011).